Flow-bearing structures of fractured rocks: Insights from hydraulic property scalings revealed by a pumping test

Nicolas Guihéneuf, A. Dausse, Jean-Raynald de Dreuzy, B. L. Parker

Journal Pre-proofs

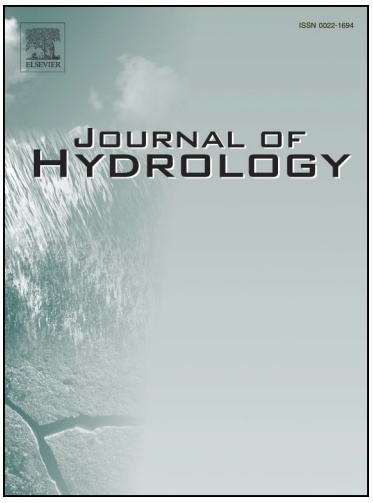

Research papers

Flow-bearing structures of fractured rocks: Insights from hydraulic property scalings revealed by a pumping test

N. Guihéneuf, A. Dausse, J.-R. Dreuzy de, B.L. Parker

PII: S0022-1694(20)31176-8
DOI: https://doi.org/10.1016/j.jhydrol.2020.125715
Reference: HYDROL 125715

To appear in: *Journal of Hydrology*

Received Date: 4 April 2020
Revised Date: 26 July 2020
Accepted Date: 26 October 2020

Please cite this article as: Guihéneuf, N., Dausse, A., Dreuzy, J.-R. de, Parker, B.L., Flow-bearing structures of fractured rocks: Insights from hydraulic property scalings revealed by a pumping test, *Journal of Hydrology* (2020), doi: https://doi.org/10.1016/j.jhydrol.2020.125715

Flow-bearing structures of fractured rocks: Insights from hydraulic property scalings revealed by a pumping test

N. Guihéneuf[a,*], A. Dausse[a], J.-R. de Dreuzy[b,c], B. L. Parker[a]

[a] *G360 Institute for Groundwater Research, College of Engineering and Physical Sciences, University of Guelph, Guelph N1G 2W1, Ontario, Canada*
[b] *Université de Rennes, CNRS, Inra, OSUR – UMS 3343, F–35000 Rennes, France.*
[c] *Université de Rennes, CNRS, Géosciences Rennes – UMR 6118, F–35000 Rennes, France.*

Abstract

A long duration pumping test conducted over 151 days in a fractured sandstone and shale formation displays a nonstandard drawdown response and anomalous pressure diffusion, which cannot be properly interpreted using existing frameworks (e.g., homogeneous, double porosity, boundary conditions, and fractal models). An alternative framework with simple geometry and more complex hydraulic properties is thus proposed to interpret such kind of drawdown responses. The analytical development allows first to demonstrate all scaling relations in this interpretation framework. Then, and most importantly, the multi-scale hydraulic test provides consistent scalings of transmissivity, T, to storativity, S, over distances ranging from 83 to 383 m in a faulted area. Drawdown analysis in several monitoring wells shows persistent decrease of transmissivity in highly channelized fracture flow structures. In one structure, the cubic dependency of transmissivity to storativity identifies a well-defined fault and also demonstrates the validity of Poiseuille flow at a scale rarely investigated. In the other structure, the linear dependency of transmissivity to storativity indicates that

*Corresponding author. Present address: Université de Rennes, CNRS, Géosciences Rennes – UMR 6118, F–35000 Rennes, France.

Email addresses: nicolas.guiheneuf@g360group.org, nicolas.guiheneuf@univ-rennes1.fr (N. Guihéneuf), amelie.dausse@g360group.org (A. Dausse), Jean-Raynald.de-Dreuzy@univ-rennes1.fr (J.-R. de Dreuzy), bparker@g360group.org (B. L. Parker)

the flow-bearing structure is the surrounding fracture network. Well-designed pumping tests combined with scaling analysis driven by geological evidence thus provide essential information on flow-bearing structures for site characterization and modeling tasks. At least for moderate to low permeable fractured rocks, the scaling of transmissivity to storativity appears to be more informative than any separate interpretation of hydraulic property scaling exponents.

Keywords: Fractional flow, Hydraulic scaling, Pressure-transient analysis, Sedimentary rocks, Fractured media, Fault

---

Highlights

- A simple framework is shown relevant to interpret nonstandard pressure responses.
- Evidence of limited fracture connectivity from a multi-scale hydraulic test.
- Decrease of transmissivity with scale of investigation observed from a well test.
- Scalings of T to S can provide essential information on flow-bearing structures.
- Despite strong heterogeneity, Poiseuille flow appears valid up to hundreds of meters.

1. Introduction

Groundwater hydrology in fractured rocks persistently faces the issue of multi-scale heterogeneity resulting in highly different flow structures (Bonnet et al., 2001; Berkowitz, 2002; Lei et al., 2017). For instance, in one extreme case, most fractures remain dry and flows are localized in a few major fracture structures over a hundred meters or more (e.g., Guihéneuf et al., 2014; Maillot et al., 2016). In the other extreme case, locally higher fracture connectivity promotes more diffuse flows in some densely fractured zones (e.g., National Research Council, 1996; de Dreuzy et al., 2012). Any situation may also occur such as isolated high fracture flows neighboring lower permeable fracture clusters (e.g., Olsson and Gale, 1995; Day-Lewis et al., 2000), or flow channeling at small scales up to some homogenization scale where flows become more evenly distributed (e.g., Bernard et al., 2006).

Identification of flow-bearing structures is the first and foremost issue for site understanding and management, especially in the context of contaminant transport and water supply (National Research Council, 1996). Any further characterization and modeling tasks rely on this identification (e.g., Kikuchi et al., 2015; Pham and Tsai, 2016; Ferré, 2017). For extremely channelized flows in a given fault (i.e., fracture or zone of fractures with appreciable relative displacement (Aydin, 1978)), characterization will focus on fault structures and their hydraulic properties (e.g., Aydin, 2000; Bense and Person, 2006; Faulkner et al., 2010; Savage and Brodsky, 2011; Bense et al., 2013; Farrell et al., 2014; Roques et al., 2014). For diffuse flows in highly connected fracture networks, single fractures become less relevant and more classical equivalent permeability concepts could be applied (e.g., National Research Council, 1996; Carrera and Martinez-Landa, 2000). It is shown here that extensively monitored well tests allow the identification of flow-bearing structures in combination with geologically-based interpretation.

Well test responses have been widely used to characterize reservoir geometries and hydraulic properties (e.g. Gringarten, 2008). In some cases, well test

responses may exhibit nonstandard drawdown explained by fractional flow models (e.g., Barker, 1988; Chang and Yortsos, 1990; Acuna and Yortsos, 1995; Hamm and Bidaux, 1996; Delay et al., 2004; Le Borgne et al., 2004; Bernard et al., 2006; Kaczmaryk and Delay, 2007; Lods and Gouze, 2008). Barker (1988) initially proposed the generalized radial flow model as a generalization of flows within 1D, 2D or 3D media. The flow dimension, n, is introduced and conceptually related to reservoir geometry (e.g., Doe, 1991). The pressure diffusion is normal in this model because the mean square radius of diffusion $\langle r^2 \rangle$ is proportional to the time, t (e.g., Acuna and Yortsos, 1995; Le Borgne et al., 2004; de Dreuzy and Davy, 2007).

In fractured rocks, however, the diffusion may be slowed down (see de Dreuzy and Davy, 2007, and references inside), and to account for this phenomenon Chang and Yortsos (1990) and Acuna and Yortsos (1995) proposed a model based on diffusion in fractal networks following O'Shaughnessy and Procaccia (1985)'s work. In this framework, the mean square radius of diffusion $\langle r^2 \rangle$ scales as t^{2/d_w} (Havlin and Ben-Avraham, 1987), where d_w refers to the anomalous diffusion exponent characterized by $d_w > 2$ for slow diffusion. An important behavior of a fractal object is that for a volume of size r, the density, ρ, is scaled such that $\rho \sim r^{d_f - d}$ with the fractal dimension, d_f, smaller than the embedded Euclidean dimension, d (e.g., Havlin and Ben-Avraham, 1987; Acuna and Yortsos, 1995). Consequently, the macroscopic fracture porosity, ϕ, decreases with distance such that $\phi \sim r^{d_f - d}$ (e.g., Acuna and Yortsos, 1995). The permeability, k, is also scaled such that $k \sim r^{d_f - d - d_w + 2}$ (e.g., Havlin and Ben-Avraham, 1987; Acuna and Yortsos, 1995; de Dreuzy and Davy, 2007). More information for generation of synthetic fractal media, such as percolation networks, and using these parameters can be found in Acuna and Yortsos (1995) and de Dreuzy and Davy (2007).

Translation of scalings in terms of generalized non-integral hydraulic dimensions has proven informative but challenging (e.g., Doe, 1991; Le Borgne et al., 2004; Bernard et al., 2006; Cello et al., 2009; Rafini and Larocque, 2009; Odling et al., 2013; Giese et al., 2017; Ferroud et al., 2018). Nonstandard pres-

sure responses may be observed in complex reservoir geometries, which can be fractal-like structures (e.g., Chang and Yortsos, 1990; Acuna and Yortsos, 1995; Lods and Gouze, 2008) or non-fractal structures (e.g., Jourde et al., 2002b; Bowman II et al., 2013). Other studies have shown that fractional flow can be developed in some 2D heterogeneous transmissivity fields, such as long-range correlated media (e.g., Walker et al., 2006; de Dreuzy and Davy, 2007). Comparing an analogous problem for heat transfer in a linear system (Carslaw and Jaeger, 1959, p. 412-415), Doe (1991) also suggested that non-integral hydraulic dimensions may arise with hydraulic properties varying as a power of distance. This latter configuration can be consistent with recurrent observations of scale-dependent hydraulic properties using experiments conducted at different locations and for various sampling scales (e.g., Vesselinov et al., 2001; Illman, 2006; Jiménez-Martínez et al., 2013; Pedretti et al., 2016).

Based on a multi-scale hydraulic test (i.e., sampling at different distances from the tested well), this study shows that nonstandard drawdown behaviors can be used to characterize the Euclidean dimension ($d = 1$ for a channel, $d = 2$ for a plane or $d = 3$ for a volume) of the flow-bearing structure and the variability of its hydraulic properties. In particular, it is demonstrated that nonstandard well test responses could, in some cases, be interpreted through an alternative framework with simple geometry and heterogeneous hydraulic properties, which are scaled from the tested well according to power-laws. After a mathematical development (Appendix A), this framework is strongly supported by the analysis of the well test data that shows consistent scalings of transmissivity, T, to storativity, S, which in turn allow the identification of flow-bearing structures corroborated with geological information. We illustrate this in a faulted sandstone and shale formation where pressure was monitored during a pumping test of 151 days with numerous responding observation wells distributed over distances ranging from 83 to 406 m.

2. Site and Dataset

2.1. The Santa Susana Field Laboratory

The Santa Susana Field Laboratory (SSFL), located in the Simi Hills in southern California, USA (Figure 1a), is a contaminated former industrial research site about 11.5 km^2 in extent, where flow and contaminant transport have been investigated since the 1980s (Cherry et al., 2009). The area is characterized by a semi-arid climate with a mean recharge of 19 mm per year (Manna et al., 2016). The Upper Cretaceous Chatworth Formation represents the main stratigraphic unit exposed at the site and consists of a composite turbidite sequence (Link et al., 1984) characterized by a typical bedding strike of N°70E and dip of approximately 25–35°NW (MWH, 2007; Cilona et al., 2015). The Chatworth Formation is primarily sandstones, referred to as mostly coarse-grained units, inter-bedded with shales and siltstones, referred to as fine-grained units (MWH, 2007; Cilona et al., 2015, 2016).

The dense fracture network consists of bedding plane fractures and different sub-vertical joint and fault populations identified from aerial photographs, outcrops and borehole geophysical and core logging (MWH, 2007; Cilona et al., 2016). Multiple sets of joints have been identified with measured lengths between 10 cm and 10 m. Two sets of joints are characterized by strikes in approximate NW–SE and NE–SW directions with dips ranging from 65° to 90° (Cilona et al., 2016). The faults can be grouped in two populations with strikes in the E–W and NE–SW directions and dips $> 70°$, for measured lengths ranging from a few meters to about 5 km (Cilona et al., 2016). Some fault zones with displacements from few to hundreds of meters, like the IEL fault (Figure 1a), may be characterized by numerous strands that link and overlap, and by relatively continuous and narrow (i.e., several decimeters) uncemented fault cores (Cilona et al., 2016).

The hydraulic conductivity of the rock matrix estimated from air permeability laboratory measurements on 96 core samples of the sandstone (i.e., regular, hard, and banded sandstone) (Hurley, 2003, and unpublished data) displayed

values ranging from 2.9×10^{-12} to 7.0×10^{-8} m s^{-1} with a geometric mean of 3.4×10^{-9} m s^{-1} (Appendix B). The matrix porosity estimated from 83 core samples of the sandstone displayed values ranging from 0.7 to 19.3 % with an arithmetic mean of 13 % (Hurley, 2003, and unpublished data). Concerning the fracture network, numerous small interval straddle-packer tests conducted in six wells illustrate transmissivity values ranging from 3.0×10^{-8} to 3.0×10^{-2} m^2 s^{-1} (Quinn et al., 2015, 2016). By taking into account the length of the straddle packer test interval (i.e., 1.5 m), the equivalent hydraulic conductivity values range from 2.0×10^{-8} to 1.9×10^{-2} m s^{-1}. From Earth tides analyses, the hydraulic conductivity values have been estimated from 9.5×10^{-9} to 3.1×10^{-6} m s^{-1} and the specific storage from 2.1×10^{-6} to 8.9×10^{-6} m^{-1}, which provide hydraulic diffusivity values between 2.9×10^{-3} and 5.0×10^{-1} m^2 s^{-1} (Allègre et al., 2016). Note that these different characterization methods investigate different scales and geological structures in the system.

2.2. Well test configuration

A finely-resolved large-scale pumping experiment performed in a major fault zone (Figure 1a) was interpreted to evaluate hydraulic property scalings of the flow-bearing structures encountered at the site. This well test was carried out in the context of groundwater characterization at the Santa Susana Field Laboratory (MWH, 2004) and data has been previously analyzed using classical analytical solutions (e.g. Theis, 1935; Moench, 1984) to extract hydraulic properties, either completely (MWH, 2004) or partially (i.e., only two observation wells) (Allègre et al., 2016). Nevertheless, all previous attempts to interpret this pumping test failed since solutions applied were not able to represent the well test behavior (Appendix B). This dataset also required additional processing before any interpretation, which was not performed in the previous analyses.

The pumping test was performed in core-hole C-1 located at the IEL fault (Figure 1a) over 151 days (MWH, 2004). An initial flow rate of about 12 m^3 h^{-1} was maintained relatively stable during 2 days, and then the flow rate was highly variable and decreased to about 7.5 m^3 h^{-1} (Figure 2a). In the

pumping well, a single packer was installed at about 487 m above mean sea level (98 m below ground surface) with a submersible pump placed below (Figure 1b). Multi-level monitoring systems using FLUTe^{TM} liners (Cherry et al., 2007) were also deployed in observation wells RD-10, RD-31, RD-53, RD-72, RD-73, HAR-1, HAR-16, and HAR-24 to measure pressure at multiple depths within each well (Figure 1b). Pressure transducers from In-Situ Inc. were used to monitor pressure at the pumping well and the twenty-one observation wells. At the observation wells (i.e., both conventional and multi-level systems), pressure transducers had a typical range of 100 psi, equivalent to about 70 m, with an accuracy of $\pm 0.08\%$ of full scale. At the pumping well, the two pressure transducers above and below the packer had a range of 250 psi, equivalent to about 176 m, with an accuracy of $\pm 0.08\%$ of full scale.

Twenty-one observation wells were monitored during this well test (MWH, 2004), but only eleven observation wells provided meaningful information (Figure 2b). Figure 2b also shows that the initial water levels in the observation wells RD-38A and RD-53 were significantly below the average initial water level of the other responding observation wells (i.e., about 14.38 m below the pumping well). Using the procedure described below, this difference will ultimately bias the results for these observation wells. RD-38A and RD-53 were therefore excluded from the analysis and all responding observation wells with similar initial conditions (i.e., RD-31, RD-35A, RD-35B, RD-72, RD-73, HAR-1, HAR-16, HAR-24, and HAR-25) were analyzed (Figure 1 and 2b). The radial distances from the pumping well for these nine observation wells range from 83 to 406 m (Figure 1b). The depths of the isolated intervals monitored using FLUTe^{TM} liners for wells RD-31, RD-72, RD-73, HAR-16, and HAR-24 are illustrated in Figure 1b. Red dots indicate an identical drawdown for each interval along the same well and green squares indicate intervals presenting different behaviors. Only intervals with specific responses and long records (i.e., not clogged or out of water during the experiment) were analyzed (Figure 1b). Note also that responses above and below the packer in the pumping well were similar during the pumping phase (Figure 2b).

3. Methods and Model

Proper drawdown analysis requires first removal of external influences (i.e., barometric and tidal effects) and flow rate variation that impact shape and amplitude of the signal. The procedure used to filter out such influences and the interpretation framework are detailed below.

3.1. Data processing

The barometric pressure and tidal effects, although relatively negligible, have been first removed following the procedures proposed by Rasmussen and Crawford (1997) and Le Borgne et al. (2004), respectively. This pumping experiment also had many interruptions and flow rate variations (Figure 2a) that required the data to be processed before any further analysis (Gringarten, 2008; Renard et al., 2009). A deconvolution procedure filtered out variations of flow rate and provided an equivalent constant rate pumping response of the reservoir (i.e., normalized response to a unit rate), which improved the interpretation (Gringarten, 2008). Among the different available algorithms (e.g., von Schroeter et al., 2004; Levitan, 2005; Al-Ajmi et al., 2008; Pimonov et al., 2009; Ahmadi et al., 2012), the deconvolution procedure in Laplace space proposed by Al-Ajmi et al. (2008) was used for convenience. In Laplace domain, the deconvolution of two functions becomes the division of their transforms, and therefore the deconvolution of the pressure response, $\overline{p_r}(p)$, to the variable flow rate, $\overline{q}(p)$, is simply (Bourgeois and Horne, 1993; Al-Ajmi et al., 2008; Ahmadi et al., 2012):

$$\overline{p_u}(p) = \frac{\overline{p_r}(p)}{p\ \overline{q}(p)}, \tag{1}$$

where $\overline{p_u}(p)$ is the unit pressure function and p is the Laplace variable. To invert Laplace transforms, the algorithm proposed by den Iseger (2006) was used because of its demonstrated robustness for transient fluid-flow problems (Al-Ajmi et al., 2008).

To transform real data into Laplace space, the linear piecewise approximation developed by Romboutsos and Stewart (1988) was used as proposed

by several authors (Bourgeois and Horne, 1993; Al-Ajmi et al., 2008; Stewart, 2011). The algorithm of Romboutsos and Stewart (1988) can be applied to interpolate both the flow rate and pressure response (Bourgeois and Horne, 1993; Al-Ajmi et al., 2008; Stewart, 2011). Note that a running mean was applied to partially remove the noise in the flow rate measurements (Figure 3a), which may be linked to measurement errors (accuracy of ±3% for the flow meter used (MWH, 2004)). The Laplace transform of a sampled function $f(t)$ is written as:

$$\overline{f}(p) = \frac{f_0}{p} + \sum_{i=0}^{n-1} \frac{f_{i+1} - f_i}{t_{i+1} - t_i} \frac{e^{-p\,t_i} - e^{-p\,t_{i+1}}}{p^2} + \frac{f_n - f_{n-1}}{t_n - t_{n-1}} \frac{e^{-p\,t_n}}{p^2}, \qquad (2)$$

where f_i corresponds to the value at time t_i. As deconvolution is an ill-conditioned problem and may provide oscillations at late times due to small errors in input data, a 1D Gaussian kernel filter was also used to smooth results as proposed by Ahmadi et al. (2012). Except for the early-time data (i.e., less than 10^4 seconds), for which the procedure had no impact due to the insufficient temporal resolution of the flow rate measurements, the deconvolution significantly improved the signal by partially or completely removing the effect of flow rate variability (Figures 3b and c). In particular, the procedure allowed correction for the general decreases in flow rate over the duration of the test, which is an important step to properly extract the flow pattern using the derivative, s', of the drawdown, s (Bourdet et al., 1989; Gringarten, 2008; Renard et al., 2009).

3.2. Interpretation framework

The interpretation framework presented here is based on previous works related to fractional flow (e.g. Barker, 1988; Acuna and Yortsos, 1995; Le Borgne et al., 2004) but differs from each by assuming simple geometry and heterogeneous hydraulic properties. As demonstrated here, this framework appears more rational for the interpretation of nonstandard drawdown responses. The mathematical development leading to the relations presented in the following is detailed in Appendix A.

The general differential diffusion equation accounting for simple geometries of flow-bearing structure describing flow in radial coordinates is (e.g., O'Shaughnessy and Procaccia, 1985; Chang and Yortsos, 1990; Delay et al., 2004; Lods and Gouze, 2008):

$$S(r)\frac{\partial s}{\partial t} = \frac{1}{r^{d-1}}\frac{\partial}{\partial r}\left(T(r)r^{d-1}\frac{\partial s}{\partial r}\right), \tag{3}$$

where T [L^2 T^{-1}] is transmissivity, S [-] is the storativity, s [L] is the head drawdown, r [L] is the radial distance from the withdrawal well, and d is a classical Euclidean dimension equal to 1, 2, or 3, which respectively correspond to a channel, a plane, or a volume. $T(r)$ and $S(r)$ denote scale-dependency related to the distance r from the well. To remind, a nonstandard drawdown response refers here to a drawdown characterized by a derivative following a power-law over several orders of magnitude in time, and diverging from classical 1D, 2D, and 3D flow regimes. To satisfy this fundamental condition, both transmissivity and storativity have to be scaled following power-laws. Other distributions would not necessarily produce non-integral hydraulic dimensions as is the case for multivariate-Gaussian permeability fields (e.g., Walker et al., 2006; de Dreuzy and Davy, 2007; Cello et al., 2009). For 2D multivariate-Gaussian fields, pressure responses rapidly converge to a radial flow regime (e.g., Walker et al., 2006; Cello et al., 2009) and thus, methods developed and validated for such a distribution of heterogeneity (e.g. Copty et al., 2011; Zech et al., 2016) cannot be applied here. In the proposed interpretation framework, hydraulic properties are thus scaled such as (equations (A.3) and (A.4) in Appendix A):

$$T \sim r^{\tau}, \tag{4}$$

$$S \sim r^{\sigma}, \tag{5}$$

where τ and σ are scaling exponents. These exponents represent an average behavior and their magnitudes indicate the degree of hydraulic heterogeneity (heterogeneous: $\neq 0$, increase: > 0 or decrease: < 0 with scale, and higher exponents mean higher heterogeneity). Hence, the geometrical dimension of the

flow-bearing structure and scalings of transmissivity and storativity control the pressure diffusion in the system. Like previous works (e.g., O'Shaughnessy and Procaccia, 1985; Acuna and Yortsos, 1995; Le Borgne et al., 2004; de Dreuzy and Davy, 2007), dimensional analysis and conservation arguments show that the drawdown response at distance r is of the form (equation (A.25) in Appendix A):

$$s(r,t) = s_e(r)\Gamma\left(-\nu, \frac{t_c(r)}{t}\right), \tag{6}$$

where $s_e(r)$ [L] is the characteristic amplitude of the reference drawdown profile at the distance r, $t_c(r)$ [T] is the characteristic diffusion time at the distance r, $\Gamma(x,y)$ is the complementary incomplete Gamma function representing the scaling function for an infinitesimal source and an infinite flow region, and ν represents the shape of the drawdown curve. This parameter can be deduced from the drawdown derivative s' (Bourdet et al., 1989) as $s' \sim t^{\nu}$, and is related to the Euclidean dimension and scaling exponents (see equation (A.12) in Appendix A).

For a configuration without scaling (i.e., $\tau = 0$ and $\sigma = 0$), drawdown responses are characterized by $s' \sim t^{0.5}$ for $d = 1$ (i.e., linear flow), $s' \sim t^{0}$ for $d = 2$ (i.e., radial flow), and $s' \sim t^{-0.5}$ for $d = 3$ (i.e., spherical flow) (e.g. Barker, 1988) (Figure 4). For configurations with scaling, the characteristic amplitude, s_e, and time, t_c, of the drawdown responses have simple scale dependencies (equations (A.26) and (A.27) in Appendix A):

$$s_e \sim r^{2-d-\tau}, \tag{7}$$

$$t_c \sim r^{2+\sigma-\tau}. \tag{8}$$

The scaling of the amplitude (equation (7)) is a function of the Euclidean dimension and transmissivity scaling while the scaling of the diffusion time (equation (8)) depends on the ratio of storativity to transmissivity scalings but not on the embedding Euclidean dimension. These relations are consistent with classical models where the characteristic amplitude is a function of the transmissivity and the characteristic time of the hydraulic diffusivity (e.g. de Marsily,

1986, p. 162). Complementary information related to characteristic amplitude and time in the context of fractal models can be found in Le Borgne et al. (2004).

Following the procedure proposed by Le Borgne et al. (2004), the scalings of s_e and t_c can be extracted first by estimating the values for each observation well by fitting the general solution (6) to their drawdown curve using, for instance, the least-squares method; and second by plotting all individual values of s_e and t_c in a log-log diagram as a function of distance, r, from the pumping well. Figure 4 presents a workflow diagram summarizing the full procedure.

Additional geological arguments on the Euclidean dimension are necessary to relate the transmissivity and storativity scalings to those of the observed drawdown amplitude and diffusion time. For fractured rocks, a linear flow geometry characterized by $d = 1$ can be caused by a vertical well crossing a channel, a vertical fracture or a vertical zone of fractures (e.g., Cinco-Ley and Samaniego-V, 1981; Karasaki et al., 1988; Gringarten, 2008). An Euclidean dimension of one can either represent straight or curved structures. A radial flow geometry ($d = 2$) can be caused by a vertical well crossing one or several horizontal fractures or a horizontal formation with relatively well-connected fracture network (e.g., Cinco-Ley and Samaniego-V, 1981; Karasaki et al., 1988). Finally, a spherical flow geometry ($d = 3$) can be caused when the well crosses a small interval in a dense and well-connected fracture network (e.g., Barker, 1988; Karasaki et al., 1988). In some configurations, an appropriate Euclidean dimension could be challenging to define, which in turn could also result in a non-unique interpretation.

4. Results

A preliminary investigation of the drawdown signal shows two distinct hydraulic responses (Figure 5). In a first category, drawdowns of RD-35B, RD-31, HAR-24, and HAR-16 follow the late-time behavior of the pumping well response. They are characterized by a persistent scaling of $s' \sim t^{0.80}$ over several

orders of magnitude (Figure 5b). In the second category, drawdowns of RD-35A, RD-73, RD-72, HAR-25, and HAR-1 have delayed responses and a different behavior (Figure 5a), where $s' \sim t^{0.98}$ (Figure 5b). Furthermore, normalizing time according to r^2 (Figure 5a) did not display superimposed curves, which illustrates anomalous pressure diffusion. Consequently, this well test displays a clear nonstandard drawdown response and cannot be interpreted using classical analytical solutions generally used for these systems (Appendix B). Double-porosity solutions converge to a radial flow regime (i.e., a plateau on drawdown derivative) and no-flow boundaries conditions develop either $s' \sim t^{0.5}$ or $s' \sim t^{1}$ depending on the number of boundaries (Appendix B).

Hydraulic responses are strongly controlled by the structure intersected. Indeed, two observation wells, RD-35A and RD-35B, located in the same area and at approximately the same distance from the pumping well (83 and 91 m, respectively; Figure 1a), are in different categories (Figure 5b). RD-35A, which was drilled to 34 m below ground surface (Figure 1b), is classified in the second category while RD-35B, which was drilled to 100 m (Figure 1b), is in the first category. These observations of two different responses at nearly the same location but different depth intervals suggest the intersection of two structures of different hydraulic properties, referred to hereafter as structure 1 and 2 for the first and second categories, respectively.

The shape of the drawdown curves characterized by $s' \sim t^{0.80}$ and $s' \sim t^{0.98}$, extracted from the behavior observed on the drawdown derivatives (Figure 5b) of the closest observation wells (i.e., RD-35A and RD-35B), were fixed hereafter to analyze the responses using the equation (6). In other words, the parameter ν was fixed to $\nu = 0.8$ for structure 1 and to $\nu = 0.98$ for structure 2, which implies that only the characteristic amplitude, s_e, and time, t_c, were estimated using the least-squares method. Trust Region Reflective algorithm implemented in Python was used to solve the least-squares problem. Residuals were simply calculated using differences between data and model curves without involving a logarithmic comparison. This procedure gives more importance to intermediate and late-time data, where the shapes of drawdown curves are stabilized. This

choice excludes strong influences of measurement uncertainties (i.e., uncertainty of pressure transducers and lack of flow-rate data at the beginning of the test) and local heterogeneities, which impacted early-time data from the test. Table 1 summarizes the values of s_e and t_c obtained for each observation well estimated using equation (6). The normalized root-mean-square deviation values, $NRMSD$, calculated between 0.37 and 1.42 %, indicate very good fits to the solution.

The corresponding spatial analysis displays consistent scalings of the characteristic amplitude and time, with $s_e \sim r^{2.26}$ and $t_c \sim r^{2.82}$ (Figure 6, blue squares) for structure 1 (i.e., $s' \sim t^{0.80}$), and $s_e \sim r^{2.08}$ and $t_c \sim r^{2.12}$ (Figure 6, red dots) for structure 2 (i.e., $s' \sim t^{0.98}$). Indeed, once the scalings of t_c are extracted for each structure, the scalings of s_e can be estimated using the equation (A.12) that relates the scaling exponents of s_e and t_c (equations (7) and (8)) to the parameter ν. One may observe that the scale evolution of s_e from the data appear very consistent with the power laws described by the estimated exponents. Note however that scalings of s_e and t_c correspond to global trends with three slight deviations of HAR-16$_{P11}$, RD-72$_{P6}$, and HAR-1$_{P10}$ (Figure 6), which indicate some additional degree of heterogeneity.

As classically known, a pumping test conducted in a vertical well located in a sub-vertical fault zone may produce a linear flow regime (i.e., $s' \sim t^{0.5}$) for a case without scaling (Roques et al., 2014; Dewandel et al., 2014). This behavior is also true for a well test performed in a vertical well located in a narrow corridor, a channel, or a vertical fracture (e.g., Cinco-Ley and Samaniego-V, 1981; Karasaki et al., 1988; Gringarten, 2008; Zhang et al., 2018). Using the equation (A.25), the linear flow regime can be simulated by fixing the Euclidean dimension to $d = 1$ and the scaling exponents to zero. In absence of hydraulic heterogeneity and matrix contribution, a linear flow regime is expected for the well test presented here because the vertical pumping well is located in a sub-vertical fault zone (i.e., the IEL fault). Consequently, the Euclidean dimension must be fixed to $d = 1$ to properly interpret this test. An Euclidean dimension of one is also strongly supported by the slope on the drawdown derivative (i.e.,

$s' \sim t^{0.8}$ at the pumping well), which is higher than the slope for a linear flow regime. As mentioned above, in absence of hydraulic heterogeneity, drawdown is characterized by a plateau on its derivative (i.e., $s' \sim t^0$) for an Euclidean dimension of two, and by $s' \sim t^{-0.5}$ for an Euclidean dimension of three.

Fixing $d = 1$ and using equations (7) and (8), the scaling exponents τ and σ for each structure can be estimated and correspond to $\tau = -1.26$ and $\sigma = -0.44$ for structure 1 and $\tau = -1.08$ and $\sigma = -0.96$ for structure 2. Figure 7 illustrates the normalized deconvolved drawdown, $s/[Q\, r^{2-d-\tau}]$, as a function of the normalized time, $t/r^{2+\sigma-\tau}$, and confirms the grouping of well test responses in two structures. To check if scaling exponents can be properly extracted using equation (6) for a case with two structures, a numerical simulation has been performed and is presented in Appendix C. The numerical results (Figure C.11) show that the scaling exponents can be reasonably estimated in this case due to contrasted hydraulic properties. Notice also that the pumping well response was properly reproduced by this simple numerical simulation (Figure C.11d), while this response was not included in the scaling analysis.

The hydraulic properties have been also estimated using equations (A.26), (A.27), and (A.30) for each structure (Table 2). The generalized scaled transmissivity, T_0, range from 48.3 to 106.8 $\mathrm{m}^{4-d-\tau}\ \mathrm{s}^{-1}$ for structure 1 and from 0.9 to 7.9 $\mathrm{m}^{4-d-\tau}\ \mathrm{s}^{-1}$ for structure 2. The generalized scaled storativity, S_0, range from 8.2 to 12.4 $\mathrm{m}^{2-d-\sigma}$ for structure 1 and from 25.2 to 133.5 $\mathrm{m}^{2-d-\sigma}$ for structure 2. The scaled hydraulic diffusivity, $D_0 = T_0/S_0$, range from 3.9×10^0 to 1.2×10^1 $\mathrm{m}^{2+\sigma-\tau}\ \mathrm{s}^{-1}$ for structure 1 and from 2.8×10^{-2} to 9.8×10^{-2} $\mathrm{m}^{2+\sigma-\tau}\ \mathrm{s}^{-1}$ for structure 2. Using the equation (A.30), the equivalent cylindrical hydraulic diffusivity at distance r ranges from 2.9×10^{-2} to 2.2×10^{-1} $\mathrm{m}^2\ \mathrm{s}^{-1}$ for structure 1 and from 1.4×10^{-2} to 5.0×10^{-2} $\mathrm{m}^2\ \mathrm{s}^{-1}$ for structure 2. Consequently, structure 1 is significantly more permeable and diffusive compared to structure 2.

As mentioned above, $d = 1$ is the most rational Euclidean dimension. For $d = 2$, the scaling exponents would be $\tau = -2.26$ and $\sigma = -1.44$ for structure 1 and $\tau = -2.08$ and $\sigma = -1.96$ for structure 2. For $d = 3$, the scaling

exponents would be $\tau = -3.26$ and $\sigma = -2.44$ for structure 1 and $\tau = -3.08$ and $\sigma = -2.96$ for structure 2. These higher exponents for $d = 2$ and 3 imply higher hydraulic heterogeneity to generate the observed drawdown curves (equation (A.12)) that cannot be further justified. Indeed, $d = 1$ is strongly consistent with the hydraulic signal and the geological structures as demonstrated in the next section.

5. Discussion

Based on these results, the scaling of transmissivity to storativity is shown to provide essential information on flow-bearing structures, which can be then related to site geological evidence. The limitations and advantages of the proposed methodology are then discussed.

5.1. Hydraulic property scalings

The negative values of the transmissivity scaling τ for both structures suggest a strong decrease of transmissivity with scale of investigation. The magnitude of τ (-1.08 and -1.26) shows that the heterogeneity is very high. The strong decrease of transmissivity and storativity with scale of investigation observed does not provide independent information on the fracture structure. Their relation is however highly informative. The scaling of transmissivity to storativity provides $T \sim S^3$ ($\tau \approx 3 \times \sigma$, with $T \sim r^{\tau=-1.26}$ and $S \sim r^{\sigma=-0.44}$) for structure 1 and $T \sim S$ ($\tau \approx \sigma$, with $T \sim r^{\tau=-1.08}$ and $S \sim r^{\sigma=-0.96}$) for structure 2. With a simple model of N fractures of aperture a_f presented by Guéguen and Palciauskas (1994), hydraulic properties are simply expressed as $T \sim N{a_f}^3$ and $S \sim N a_f$ (Guéguen and Palciauskas, 1994; Le Borgne et al., 2004). According to this simple model, fracture aperture a_f is the relevant parameter to obtain the relation $T \sim S^3$ for structure 1 while, for structure 2, fracture density N is the relevant parameter to obtain the relation $T \sim S$. Hence, the scale dependency of hydraulic properties could be mainly related to aperture for structure 1 and to fracture density for structure 2. The strong decrease of hydraulic properties

with scale of investigation may thus be simply related to a decrease of fracture aperture in a single fracture or zone of fractures for structure 1. For structure 2, the decrease of hydraulic properties may be simply related to a decrease of fracture density in a more dense fracture network. Although variability of fracture aperture in structure 2 is obviously not excluded, the signal still appears dominated by fracture density. Consequently, structure 1 behaves hydraulically as an idealized fault and structure 2 as a fracture network. This explanation is further confirmed with geological information on the flow-bearing structures.

5.2. Geological identification of the flow-bearing structures

The cubic relation of transmissivity to storativity (i.e., $T \sim S^3$) for structure 1 indicates strongly channelized flow within a fault, which is supported by geological information. Indeed, fault attributes (i.e., gouge, breccia, or striations) have been reported in C-1, RD-31, and RD-35B (Hurley, 2003; MWH, 2007, 2016), and the sub-vertical IEL fault zone may be characterized by numerous strands that link and overlap, with narrow and relatively continuous uncemented fault cores (Cilona et al., 2016). Drawdowns in HAR-16 and HAR-24, both away from the IEL fault, follow the same trend indicating preferential connections to the IEL fault. The cubic dependency of transmissivity to storativity shows that drawdown is controlled by channelized flows in the IEL fault, and eventually suggest that Poiseuille flow may be valid to some hundreds of meters. Poiseuille flow, although classically interpreted as a parallel plate model which leads to the cubic law (i.e., cubic relation between transmissivity and aperture), does not preclude more complex fault organizations as long as the main least-resistance to flow is an open space and not a porous-like medium (Oron and Berkowitz, 1998). The magnitude of τ (-1.26) also indicates a high heterogeneity thus a strong channeling in the fault zone.

The linear relation of transmissivity to storativity (i.e., $T \sim S$) for structure 2 indicates more diffuse flows within a fracture network. All the wells of structure 2 are within a few hundred meters from the shear zone fault, which falls into the corresponding damage zone independently estimated (Cilona et al., 2015,

2016). Even though bedding plane fractures and multiple sets of sub-vertical joints compose the surrounding fracture network (Cilona et al., 2016), the signal may be dominated by sub-vertical joints as flows appear confined within fracture zones of dimension one. This is supported by the absence of depth dependency of the drawdown revealed from multi-level monitoring systems. The confinement of flows within fracture zones of dimension one is however an indicator of limited lateral fracture connectivity. Higher fracture connectivity would be characterized by Euclidean dimension of $d = 2$ or 3. One may observe that whatever the Euclidean dimension, the relation of transmissivity to storativity remains linear for this structure.

Even though the well test was conducted in a sandstone and shale formation, the rock matrix influence appears to be negligible from the pumping signal that is also supported by other arguments. Firstly, the classical double-porosity signal (e.g., Warren and Root, 1963; Moench, 1984; Gringarten, 2008) did not appear and the drawdown did not converge to a pseudo-radial flow regime (i.e., $s' \sim t^0$) (e.g., Cinco-Ley and Samaniego-V, 1981; Gringarten, 2008). Secondly, the matrix permeability is significantly lower than the fracture network permeability, although the porosity of the rock matrix (i.e., 13 %) may be much higher than the fracture porosity (Hurley, 2003; Quinn et al., 2015, 2016). To support these arguments, Appendix B presents simple modeling scenarios showing some classical signals expected for significant matrix influence. Thirdly, a simple numerical model considering hydraulic property scalings into idealized flow-structures embedded in an impermeable matrix consistently reproduces the observed signal (Appendix C). Hydraulic property scaling is also less expected for the rock matrix.

5.3. Bias related to well location

This well test dataset shows a relatively low-permeable reservoir where ten observation wells did not display a response (Figure 1a) when a single nearby well was pumped. The signal was not transmitted likely because of limited connectivity (i.e., $d = 1$) and low permeability. Observation wells on the western

side of the shear zone fault (Figure 1a) did not respond likely because of limited connectivity and/or impeded across-fault flow due to clay rich fault core and shale smearing reducing the permeability of the shear zone (Cilona et al., 2015). Note however that some connection may persist as illustrated by the observation wells RD-38A and RD-53 located in the Woolsey Canyon fault (Figures 1 and 2).

The point from which the well test is performed in the structure induces a strong bias in the characterization of heterogeneous reservoirs (e.g., Guimerà et al., 1995; Jourde et al., 2002a; de Dreuzy and Davy, 2007). This bias, introduced by the choice of the pumping well (i.e., typically the most productive well), may be somewhat expected as the pumped well should have an observable drawdown in a long-term hydraulic test. The long-term nature of the test is necessary to facilitate a relevant analysis of the scaling of the hydraulic properties, from radius of investigation increasing over several orders of magnitude (i.e., typically from a few meters to some hundreds of meters). In a less or non-connected zone, the well test would not provide any observable drawdown and no meaningful observations.

For broadly heterogeneous media such as fractured rock studied here, hydraulic property scalings are first and foremost influenced by the location of the well in the structure rather than the mean hydraulic properties of the structure. This is typically the case for multi-fractal structures, where synthetic well tests result in any possibility of transmissivity scaling between $\tau = -1$ and $\tau = 0.5$, with mean scaling similar to that of a homogeneous medium ($\tau = 0$ in dimension $d = 2$) (de Dreuzy and Davy, 2007). In such cases, any single realization does not reveal a mean behavior but a specific characterization biased by the location of the well. Scaling from a single well test would give the same result as any other well tests only if the heterogeneity structure is a fractal, not a multi-fractal. Still, in such well-defined structures, transport scalings may be modified by boundary conditions, as it is the case for volatile fractals (Herrmann and Stanley, 1984; de Dreuzy et al., 2001). Whatever their type, regularity of fractal structures is not observed in fractured media, the scaling

of which rather comes from the correlation of fracture locations, or the organization of the largest and smallest structures according to some mechanical relaxation process (Davy et al., 2010). Consequently, one should not generalize the scaling exponents estimated here to another location at this site.

5.4. Advantages of the geological-based interpretation framework

To underline the relevance of the proposed interpretation framework with the hydraulic property scalings, results reported in this study can be alternatively analyzed according to well-discussed fractal flows originally based on diffusion in fractal structures (e.g., O'Shaughnessy and Procaccia, 1985; Havlin and Ben-Avraham, 1987; Chang and Yortsos, 1990; Acuna and Yortsos, 1995; Le Borgne et al., 2004; de Dreuzy and Davy, 2007). The fractal dimension, d_f, and the anomalous diffusion exponent, d_w, can be linked to the scaling exponents:

$$d_f = d + \sigma, \tag{9}$$

$$d_w = 2 + \sigma - \tau. \tag{10}$$

In the case of normal diffusion where $d_w = 2$, the fractal dimension has been also denoted as the generalized flow dimension, n (Barker, 1988), where $d_f = n \times d_w/2$ (e.g., Acuna and Yortsos, 1995; Le Borgne et al., 2004; de Dreuzy and Davy, 2007), which reduces to the Theis (1935) solution for $n = 2$. In this framework, the scaling of the characteristic amplitude, s_e, and time, t_c, are $s_e \sim r^{d_w - d_f}$ and $t_c \sim r^{d_w}$, respectively. The interpretation framework with the hydraulic property scalings is more appropriate here because the observed scaling of the characteristic amplitude (i.e., $s_e \sim r^{2.26}$) associated with an anomalous diffusion of $d_w = 2.82$ leads to an inconsistent fractal dimension lower than 1 (i.e., $d_f = 0.56$) for a continuous fracture network. A fractal dimension of 1 corresponds to the minimum dimension for a fracture (e.g., Acuna and Yortsos, 1995). Generalized radial flow models (Barker, 1988; Liu et al., 2016) or more advanced models based on diffusion in fractal structures (e.g.,

Chang and Yortsos, 1990; Acuna and Yortsos, 1995; Lods and Gouze, 2008) are thus inappropriate in this case.

It is proposed here that hydraulic scalings be interpreted with simple fracture geometries (i.e., $d = 1$, 2, or 3) with more complex hydraulic properties. The Euclidean dimensions of the structures should be confirmed based on the available geological knowledge. In most cases with prominent faults, the Euclidean dimension of the fault structure will be one or two depending on the respective orientations of the fault and well. An Euclidean dimension of three would only be found in more connected and dense fracture networks inconsistent with the low connectivity and transmissivity observed here. The scaling observed for structure 1 of $T \sim S^3$ is highly consistent with a fault and the negative exponents with an effective aperture that decreases away from the tested well. Structure 2 shows the confinement of flows within fracture zones of dimension one. The low dimension (i.e., $d = 1$) is a consistent indicator of the lack of connectivity. As the dimension of the geological structures (faults, joints) remains in most cases quite simply equal to an Euclidean dimension, it is proposed that the scaling identified in a well test be interpreted as the relative scaling from this given location.

The hydraulic property scaling is not only an absolute characteristic but an indication of the degree of hydraulic heterogeneity of the structure. Higher transmissivity scaling would mean higher heterogeneity. This interpretation framework is also consistent with recurrent observations of highly heterogeneous fracture apertures and transmissivities (e.g., Méheust and Schmittbuhl, 2001; Ishibashi et al., 2015).

The results obtained from this well test ultimately show that the relation of transmissivity to storativity is highly informative with respect to the nature of the hydraulically effective fractures. Well tests conducted using a network of many responsive piezometers may provide efficient hydraulic information on the fracture nature (i.e., fault and fracture network), the Euclidean dimension, and the degree of heterogeneity. Hence, the proposed interpretation framework can be a useful tool to define relevant groundwater flow models (e.g., single fracture

with heterogeneous aperture, fracture network with varying density, etc.). The extracted information (i.e., nature of flow-bearing structure, Euclidean dimension, and degree of heterogeneity) can be indeed used thereafter for predictive modeling involving different scales and boundary conditions.

6. Conclusions

Based on a multi-scale pumping experiment conducted in a fractured formation, a framework with simple geometry and heterogeneous hydraulic properties is demonstrated relevant to interpret nonstandard drawdown responses. Most importantly, the scaling of transmissivity to storativity is demonstrated to be highly informative with respect to identifying flow-bearing structures in combination with geological information, at least for moderate to low permeable fractured rocks. The analysis reveals an important decrease of hydraulic properties from the tested well to some hundreds of meters, which suggests a highly heterogeneous reservoir. The observed responses can be interpreted in terms of decrease of fracture density in the surrounding fracture network with limited connectivity and of decrease of fracture aperture in the well-identified fault. The cubic relation of transmissivity to storativity for the fault suggests that Poiseuille flow may be valid at a scale rarely investigated (i.e., about 400 m). Although individual values of the scaling exponents are representative of a specific characterization, well-designed hydraulic tests and scaling analysis may provide unique information on the flow-bearing structures and additional capacity for modeling.

Acknowledgments

This study was funded by the site owner, The Boeing Company, and the Natural Sciences and Engineering Research Council (NSERC) of Canada through an Industrial Research Chair to Beth L. Parker. The authors are grateful to the site owner and their consultants Nicholas Johnson, Steven Reiners, and

Richard Andrachek from MWH Americas Inc. (now Stantec Inc.) for collecting and providing the dataset. Data are available upon request at `https://doi.org/10.5683/SP2/S9MUQO`. The editors and the anonymous reviewers are also warmly thanked for their thoughtful comments.

618 ## Figures

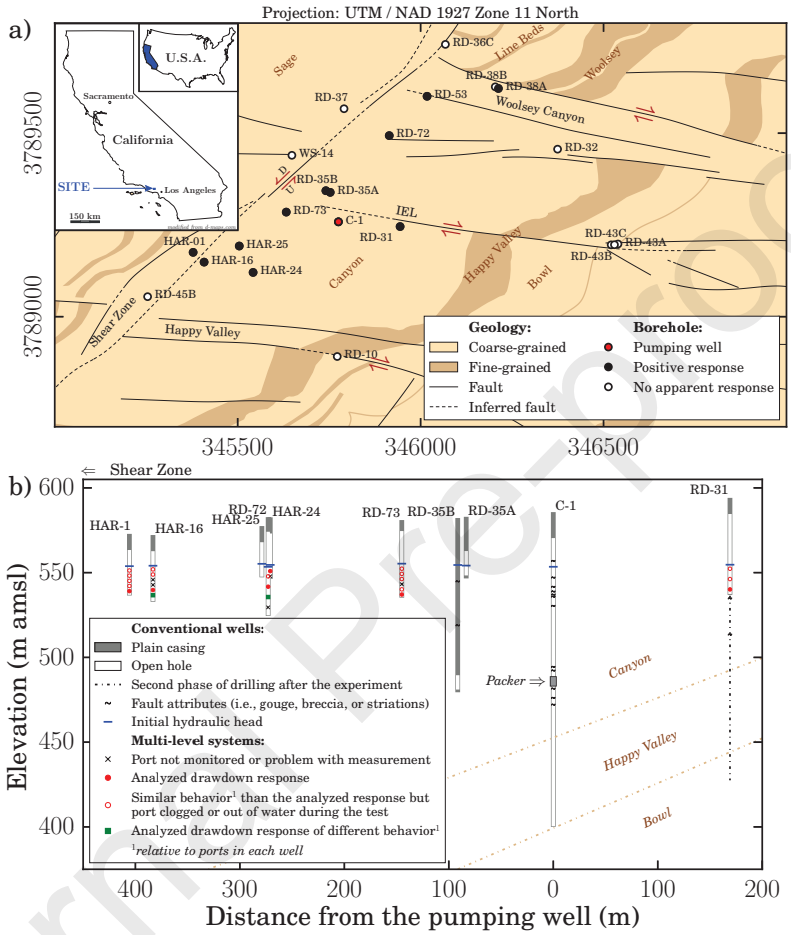

Figure 1: a) Boreholes location and geological map of the SSFL (modified after MWH (2007); Cilona et al. (2015, 2016)). b) Configuration of observation wells analyzed and distances investigated.

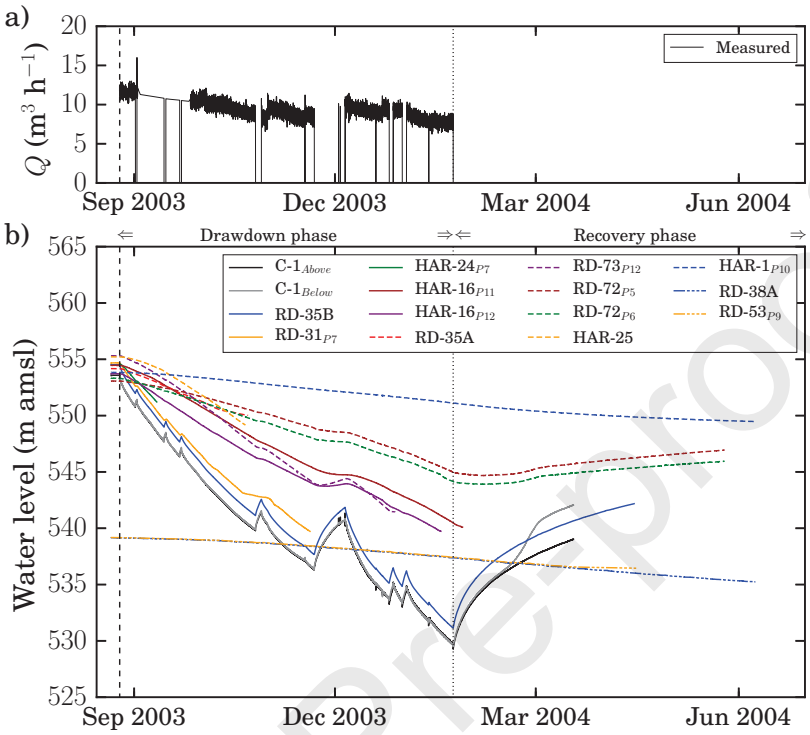

Figure 2: a) Measured flow rate with an accuracy of ±3% for the flow meter used (MWH, 2004). b) Water level measurements for the observation wells with response to the pumping test. Note that the initial water level in RD-38A and RD-53$_{P9}$ were below the initial water level in the pumping well with a difference of about 14.38 m.

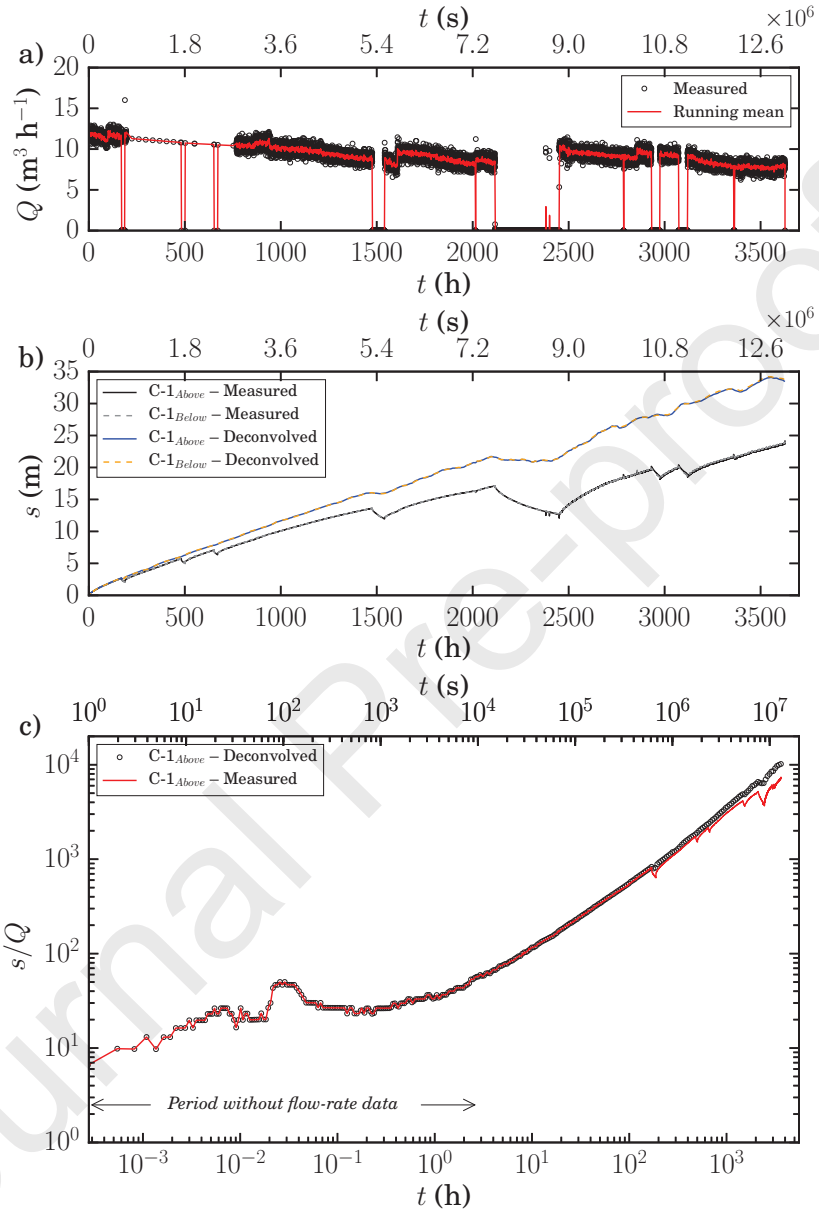

Figure 3: a) Measured flow rate smoothed with a running mean (red line). The running mean removed partially the noise but kept the pumping interruptions. b) Measured and deconvolved drawdown at C-1 pumping well above and below the packer. Note that the deconvolved drawdown are normalized to the initial flow rate. c) Measured and deconvolved drawdown at C-1 pumping well above the packer in log-log diagram, both normalized to the unit-rate response or equivalent (i.e. normalized by the mean initial flow rate for the measured drawdown). Because the temporal resolution of the flow-rate measurement was not sufficient, the deconvolution had no impact at the early times.

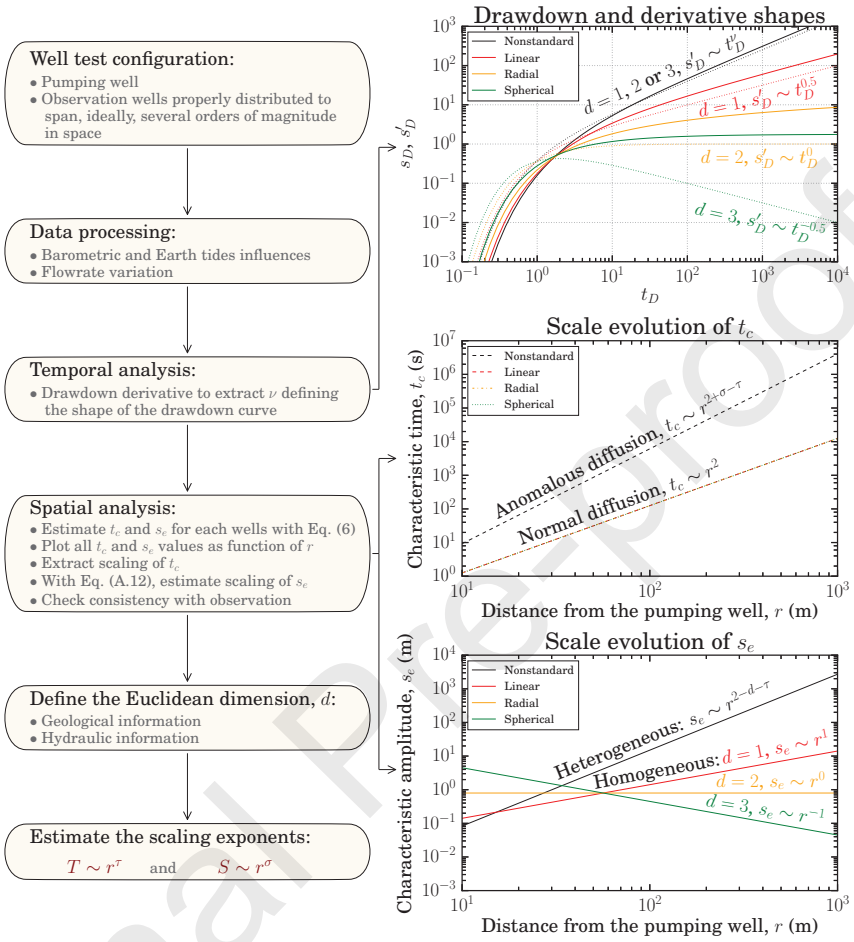

Figure 4: Workflow diagram summarizes the procedure to estimate scaling exponents of hydraulic properties from a well test. Behaviors for linear, radial, and spherical flow geometry with normal diffusion in homogeneous media are illustrated (e.g. Barker, 1988) as references in order to compare with nonstandard drawdown responses with anomalous diffusion in heterogeneous media.

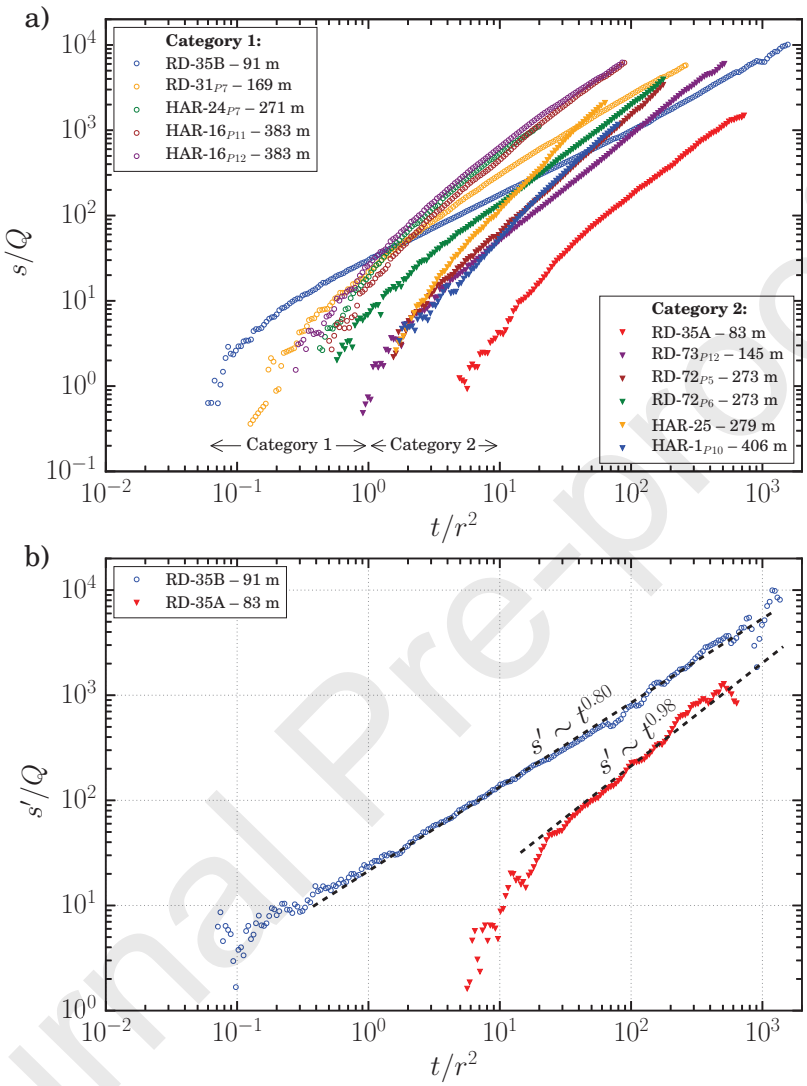

Figure 5: a) Specific drawdown (i.e., deconvolved and normalized to a unit rate) for all responding observation wells in log-log diagram. Time is normalized according to the square of the distance, r, to the pumping well. Two categories of observation wells can be extracted according to the normalized arrival time and the shape of the drawdown curves. One may observe that the classical normalization for normal pressure diffusion is inappropriate since drawdown curves are not superimposed. b) Specific drawdown derivatives calculated using Bourdet et al. (1989)'s method of RD-35B (category 1) and RD-35A (category 2), the closest observation wells from the pumping well C-1. The slopes observed on derivatives were used to fix the parameter ν for each structure.

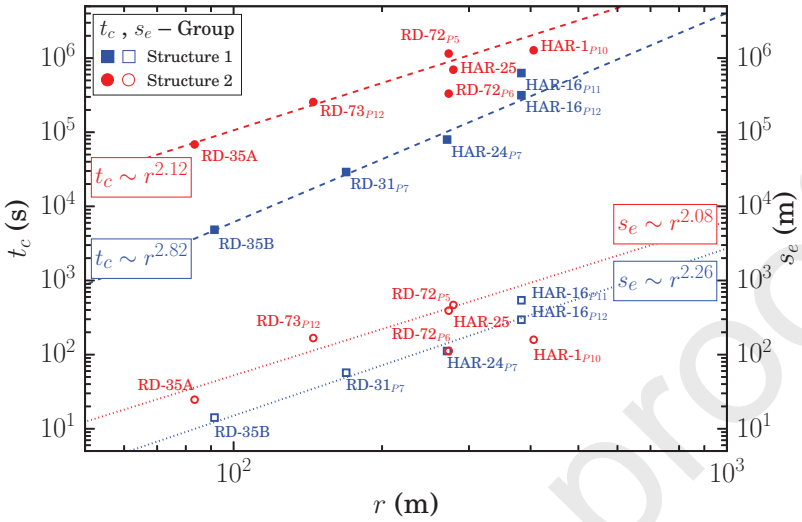

Figure 6: Characteristic time, t_c, and amplitude, s_e, as a function of the distance, r, to the pumping well for both structures (Table 1). For structure 1, $t_c \sim r^{2.82}$ and $s_e \sim r^{2.26}$ and for structure 2, $t_c \sim r^{2.12}$ and $s_e \sim r^{2.08}$. Once these exponents are estimated, the hydraulic property scaling exponents can be next calculated by fixing the Euclidean dimension. Using $d = 1$, the exponents are $\sigma = -0.44$ and $\tau = -1.26$ for structure 1 and $\sigma = -0.96$ and $\tau = -1.08$ for structure 2.

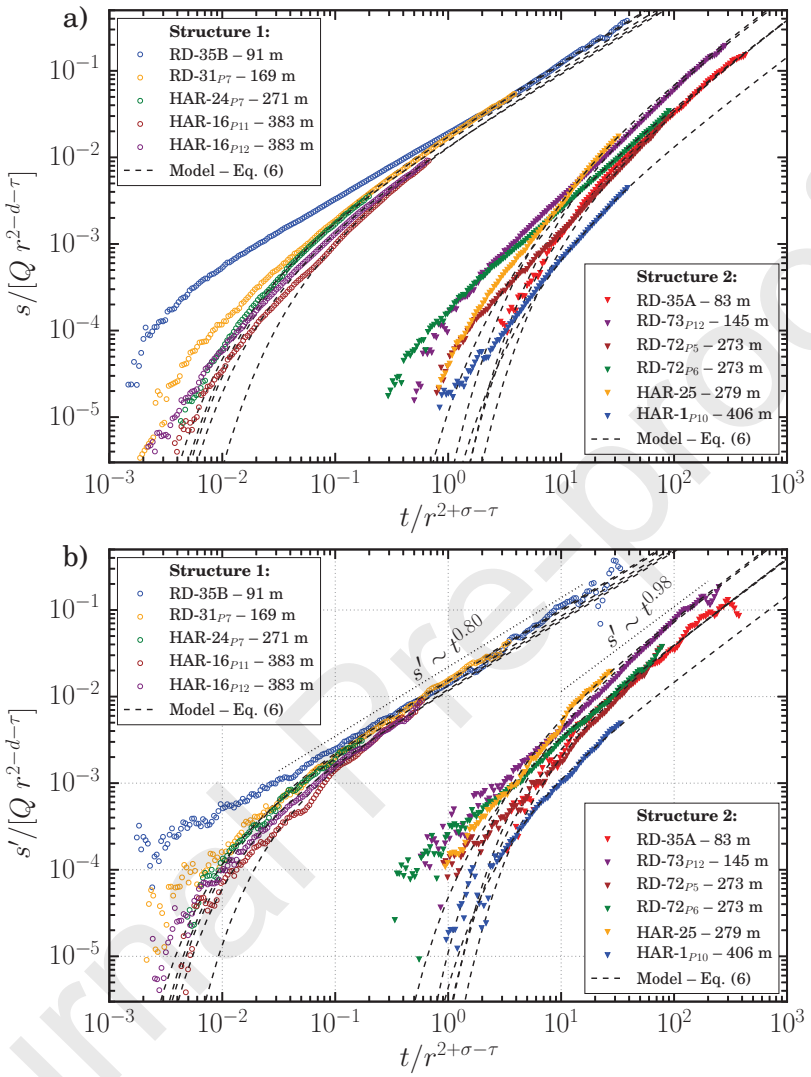

Figure 7: a) Drawdowns, s, and b) derivatives, s', using Bourdet et al. (1989)'s method, with fits of the equation (6) using the least-squares method. Drawdowns and derivatives are both normalized in time and amplitude according to the respective scaling exponents of each structure, which are $t_c \sim r^{2+\sigma-\tau=2.82}$ and $s_e \sim r^{2-d-\tau=2.26}$ for structure 1 and $t_c \sim r^{2+\sigma-\tau=2.12}$ and $s_e \sim r^{2-d-\tau=2.08}$ for structure 2.

Tables

Table 1: Parameters for each observation well, where r is the distance from the pumping well, t_c is the characteristic time, s_e is the characteristic drawdown amplitude, ν is the slope of drawdown derivative. Note that ν was fixed from derivative analysis to estimate t_c and s_e from the equation (6) using the least-squares method. The normalized root-mean-square deviation, $NRMSD$, which was calculated using $NRMSD = \sqrt{\frac{\sum_{i=1}^{N}(y_i - y_{m_i})^2}{N}}/(y_{max} - y_{min})$, is expressed in percentage.

Name	Str.	r (m)	t_c (h)	s_e (m)	ν (-)	$NRMSD$ (%)
RD-35B		91.5	1.34	14.15		0.94
RD-31$_{P7}$		169.1	8.07	57.02		0.37
HAR-24$_{P7}$	1	270.9	22.12	111.79	0.80	0.43
HAR-16$_{P11}$		383.2	174.59	541.13		0.69
HAR-16$_{P12}$		383.2	87.67	295.50		0.54
RD-35A		83.4	19.01	24.67		1.32
RD-73$_{P12}$		145.0	70.95	167.37		0.75
RD-72$_{P5}$	2	272.9	319.80	391.87	0.98	1.42
RD-72$_{P6}$		272.9	92.16	112.03		1.00
HAR-25		278.9	193.72	467.79		0.87
HAR-1$_{P10}$		405.7	354.13	158.65		0.81

Table 2: Parameters obtained for each observation well using equations (A.26), (A.27), and (A.30). T_0 is the generalized scaled transmissivity, S_0 is the generalized scaled storativity, D_0 is the scaled hydraulic diffusivity (i.e., $D_0 = T_0/S_0$), and $D(r)$ is the equivalent cylindrical hydraulic diffusivity at distance, r.

Name	Str.	T_0 ($m^{4-d-\tau}$ s^{-1})	S_0 ($m^{2-d-\sigma}$)	D_0 ($m^{2+\sigma-\tau}$ s^{-1})	$D(r)$ (m^2 s^{-1})
RD-35B	1	72.8	8.2	8.9×10^{0}	2.2×10^{-1}
RD-31$_{P7}$		72.3	8.7	8.4×10^{0}	1.2×10^{-1}
HAR-24$_{P7}$		106.8	9.3	1.2×10^{1}	1.2×10^{-1}
HAR-16$_{P11}$		48.3	12.4	3.9×10^{0}	2.9×10^{-2}
HAR-16$_{P12}$		88.4	11.4	7.7×10^{0}	5.8×10^{-2}
RD-35A	2	1.9	49.3	3.8×10^{-2}	2.3×10^{-2}
RD-73$_{P12}$		0.9	26.5	3.3×10^{-2}	1.8×10^{-2}
RD-72$_{P5}$		1.4	49.7	2.8×10^{-2}	1.4×10^{-2}
RD-72$_{P6}$		4.9	50.0	9.8×10^{-2}	5.0×10^{-2}
HAR-25		1.2	25.2	4.9×10^{-2}	2.5×10^{-2}
HAR-1$_{P10}$		7.9	133.5	5.9×10^{-2}	2.9×10^{-2}

Appendix A. Mathematical derivation of the solution

Mathematical development leading to the relations presented in the proposed interpretation framework is detailed here. Although the mathematical formalism is closely related to models based on diffusion in fractal structure (e.g. Lods and Gouze, 2008), the assumptions are different. This development was realized according to the hydraulic head to consider both injection and withdrawal of water from a well. The relation between hydraulic head and drawdown is simply defined such as:

$$s(t) = h(t=0) - h(t). \tag{A.1}$$

Traditional diffusion equation generalizing the classical Euclidean geometry in radial coordinates is (e.g., O'Shaughnessy and Procaccia, 1985; Chang and Yortsos, 1990; Delay et al., 2004; Lods and Gouze, 2008):

$$S(r)\frac{\partial h}{\partial t} = \frac{1}{r^{d-1}}\frac{\partial}{\partial r}\left(T(r)r^{d-1}\frac{\partial h}{\partial r}\right), \tag{A.2}$$

where T [$\mathrm{L}^2\ \mathrm{T}^{-1}$] is transmissivity, S [-] is the storativity, h [L] is the hydraulic head, r [L] is the radial distance from the injection/withdrawal well, and d is the Euclidean dimension. $T(r)$ and $S(r)$ denote dependence of transmissivity and storativity to the distance r from the tested well. To develop nonstandard responses as defined here, and consistently with previous works (e.g., Acuna and Yortsos, 1995; Delay et al., 2004; de Dreuzy and Davy, 2007; Lods and Gouze, 2008), these scale-dependencies have to be represented by power-laws:

$$T(r) = T_0 r^{\tau}, \tag{A.3}$$

$$S(r) = S_0 r^{\sigma}, \tag{A.4}$$

where τ and σ are scaling exponents, T_0 [$\mathrm{L}^{4-d-\tau}\ \mathrm{T}^{-1}$] is the generalized scaled transmissivity, S_0 [$\mathrm{L}^{2-d-\sigma}$] is the generalized scaled storativity, which are both constant values. The introduction of hydraulic property scalings in equation (A.2) results in heterogeneous systems and the diffusion equation becomes:

$$\xi\frac{\partial h}{\partial t} = \frac{1}{r^{d-1+\sigma}}\frac{\partial}{\partial r}\left(r^{d-1+\tau}\frac{\partial h}{\partial r}\right), \tag{A.5}$$

with $\xi = S_0/T_0$. The mass balance differential equation at the tested well describing the exchange between the well and the reservoir is (e.g., Lods and Gouze, 2008):

$$C_w \frac{\partial h_w}{\partial t} = \alpha_d r_w^{d-1} \left(T(r) \frac{\partial h}{\partial r} \right)_{r=r_w} + Q(t), \tag{A.6}$$

where h_w [L] is the hydraulic head at the well (i.e., $h(r = r_w, t) = h_w(t)$), C_w [L^2] is the well-bore storage (i.e., $C_w = 2\pi r_c^2$, where r_c is the well casing), r_w [L] is the radius of the well, Q [L^3 T^{-1}] is the flow rate, and $\alpha_d = 2\pi^{d/2}/\Gamma\,(d/2)$ corresponding to the area of a unit sphere in d dimensions (e.g., Barker, 1988; Lods and Gouze, 2008), where $\Gamma\,(x)$ is the Gamma function. For linear, radial, and spherical flow geometries, $\alpha_d = 2, 2\pi, 4\pi$, respectively (e.g., Barker, 1988, Table 1). Equation (A.6) in developed form becomes:

$$C_w \frac{\partial h_w}{\partial t} = T_0 \alpha_d r_w^{d-1+\tau} \frac{\partial h}{\partial r}\bigg|_{r=r_w} + Q(t). \tag{A.7}$$

The initial boundary condition assumes the hydraulic head equals zero in the system:

$$h(r, t = 0) = 0, \tag{A.8}$$

and for an infinite flow region:

$$\lim_{r \to \infty} h(r, t) = 0. \tag{A.9}$$

Using the initial condition (A.8), and applying Laplace transform to the equation (A.5) with respect to time, we obtain:

$$\xi p \bar{h} r^{\sigma - \tau} = \frac{(d - 1 + \tau)}{r} \frac{d\bar{h}}{dr} + \frac{d^2 \bar{h}}{dr^2}, \tag{A.10}$$

where p is the Laplace variable. The general solution of this equation is of the form:

$$\bar{h} = r^{\alpha\nu} \left[C_1 K_\nu(\beta r^\alpha) + C_2 I_\nu(\beta r^\alpha) \right], \tag{A.11}$$

with C_1 and C_2 are functions that need to be determined using the boundary conditions, K and I are the modified Bessel functions of the second and first kind, respectively, and the other parameters are defined as follows:

$$\nu = \frac{2 - d - \tau}{2 + \sigma - \tau}, \tag{A.12}$$

$$\alpha = \frac{2+\sigma-\tau}{2}, \tag{A.13}$$

$$\beta = \frac{\sqrt{\xi p}}{\alpha}. \tag{A.14}$$

The boundary condition (A.9) leads to $C_2 = 0$, which simplifies the solution to:

$$\bar{h} = r^{\alpha\nu} C_1 K_\nu(\beta r^\alpha). \tag{A.15}$$

The Laplace transform of (A.7) is:

$$C_w p\bar{h}_w = T_0 \alpha_d r_w^{d-1+\tau} \left.\frac{d\bar{h}}{dr}\right|_{r=r_w} + \bar{Q}, \tag{A.16}$$

with $\bar{Q} = Q/p$ for a constant flow rate. Taking the derivative of equation (A.15), which is:

$$\frac{d\bar{h}}{dr} = -C_1 \beta\alpha r^{\alpha-1} r^{\alpha\nu} K_{\nu-1}(\beta r^\alpha), \tag{A.17}$$

the equation (A.16) becomes:

$$C_w p\bar{h}_w = \frac{Q}{p} - C_1 T_0 \alpha_d \beta\alpha r_w^{\frac{d+\sigma}{2}} K_{\nu-1}(\beta r_w^\alpha). \tag{A.18}$$

The objective here is to obtain the solution for an infinitesimal source. In this case, $C_w = 0$ and r_w tends to zero. Taking properties of the modified Bessel function of the second kind, which are:

$$K_{-x}(z) = K_x(z) \quad z > 0, \tag{A.19}$$

and

$$\lim_{z\to 0} z^x K_x(z) = 2^{x-1}\Gamma(x) \quad z > 0, \tag{A.20}$$

we obtain the function C_1:

$$C_1 = \frac{Q}{pT_0\alpha_d\beta^\nu\alpha 2^{-\nu}\Gamma(1-\nu)}. \tag{A.21}$$

Injecting (A.21) in the equation (A.15), one may notice that the solution is of the form:

$$\bar{h} = Dp^{-1-\frac{\nu}{2}} K_\nu(\beta r^\alpha), \tag{A.22}$$

with

$$D = \frac{Qr^{\alpha\nu}}{T_0\alpha_d\xi^{\frac{\nu}{2}}\alpha^{1-\nu}2^{-\nu}\Gamma(1-\nu)}, \tag{A.23}$$

which can be easily inverted to time domain using:

$$L\left\{\frac{1}{2}\left(\frac{z}{2}\right)^x\Gamma\left(-x,\frac{z^2}{4t}\right)\right\} = p^{-1-\frac{x}{2}}K_x(z\sqrt{p}), \tag{A.24}$$

where $\Gamma(x,y)$ is the complementary incomplete Gamma function. Consequently, the solution in time domain is:

$$h(t) = \frac{Qr^{2\alpha\nu}}{2T_0\alpha_d\alpha\Gamma(1-\nu)}\Gamma\left(-\nu,\frac{S_0r^{2\alpha}}{4tT_0\alpha^2}\right). \tag{A.25}$$

This solution in pumping configuration can be written in the form presented in equation (6) with:

$$s_e(r) = \frac{Qr^{2-d-\tau}}{T_0\alpha_d(2+\sigma-\tau)\Gamma(\frac{d+\sigma}{2+\sigma-\tau})}, \tag{A.26}$$

and

$$t_c(r) = \frac{S_0r^{2+\sigma-\tau}}{T_0(2+\sigma-\tau)^2}. \tag{A.27}$$

Using equations (A.26) and (A.27), the generalized scaled transmissivity, T_0, and storativity, S_0, can be calculated. Along the lines of Lods and Gouze (2004), the equivalent cylindrical transmissivity, T [$\mathrm{L}^2\ \mathrm{T}^{-1}$], and storativity, S [$-$], at the distance r can be also approximated using:

$$T_0\alpha_d r^{d-1+\tau} = T(r)2\pi r, \tag{A.28}$$

$$S_0\alpha_d r^{d-1+\sigma} = S(r)2\pi r. \tag{A.29}$$

Note that these equations may be only valid for $d = 2$ and $d = 3$. For $d = 1$, because the area open to flow is generally difficult to estimate (Karasaki et al., 1988), only the equivalent cylindrical hydraulic diffusivity, D [$\mathrm{L}^2\ \mathrm{T}^{-1}$], can be properly evaluated at the distance r with:

$$D(r) = \frac{T_0r^{\tau}}{S_0r^{\sigma}}. \tag{A.30}$$

Appendix B. Fracture *vs* matrix, and no-flow boundaries

To check that matrix influences can be ignored for this well test, different simple modeling scenarios have been evaluated. The first scenario (SP_m) (Figure B.8, left) represents the classical radial flow model accounting for well-bore storage (Papadopulos and Cooper, 1967) with the average hydraulic conductivity estimated for sandstone ($K_g = 3.4 \times 10^{-9}$ m s^{-1}, the geometric mean) obtained from Hurley (2003) and unpublished data (Figure B.8, right). The second scenario (SP_f) displays the same model using fracture transmissivity ($T_f = 6.0 \times 10^{-2}$ m^2 s^{-1}) roughly estimated at the vicinity of the pumping well, and converted into hydraulic conductivity ($K_f = 4.0 \times 10^{-4}$ m s^{-1}) based on the saturated length of the well (i.e., 150 m). The third and fourth scenario represent behaviors of a double porosity model (Moench, 1984) for slab (DP_{Sl}) and spherical blocks (DP_{Sph}) using previous estimated parameters for fracture and matrix. More information concerning definitions of slab and spherical blocks can be found in Moench (1984). In these models, the average half thickness or the diameter of block matrix is assumed to be 5 m, the hydraulic conductivity of fracture system is $K_f = 4.0 \times 10^{-4}$ m s^{-1}, the hydraulic conductivity of the matrix block is $K_m = 3.4 \times 10^{-9}$ m s^{-1}, the specific storage of fracture system is $S_s = 1.0 \times 10^{-7}$ m^{-1}, the specific storage of the matrix block is $S_{sm} = 1.0 \times 10^{-5}$ m^{-1}, and the fracture skin is $s_f = 1.0$. The three latter parameters have been arbitrarily set, but they only impact the shape of the derivative for double-porosity systems (i.e., the V-shape). These simple modeling scenarios highlight that, first, all these models failed to represent the drawdown behavior, second, well-bore storage appears to be relatively negligible at early-time data, and third, matrix influences can be neglected for the analyzed well test.

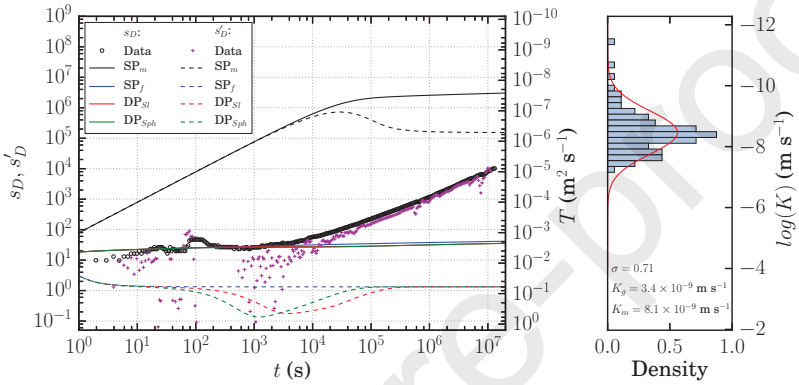

Figure B.8: Left diagram: normalized drawdowns, s_D, and derivatives, s'_D, for data at the pumping well and modeling scenarios for single porosity (SP), using one classical radial flow solution (Papadopulos and Cooper, 1967), and double porosity (DP), using another classical solution (Moench, 1984). Double porosity scenarios were simulated for slab (DP$_{Sl}$) and spherical blocks (DP$_{Sph}$) (Moench, 1984). Relation between the drawdown derivative for radial flow model, characterized by a plateau in log-log diagram, and the transmissivity is provided using $T = Q/[4\pi s']$ (Renard et al., 2009). Right diagram: matrix hydraulic conductivity measurements from rock cores analysis (Hurley, 2003, and unpublished data). Relationship between the transmissivity and hydraulic conductivity were based on the full saturated length of the pumping well (i.e., 150 m).

To evaluate influences of no-flow boundaries at intermediate and late-time behaviors, three models with different boundary conditions have been simulated using well-images theory (Figure B.9). A skin factor of 1 was assumed at the pumping well. The hydraulic conductivity and specific storage were fixed to $K = 4.0 \times 10^{-4}$ m s^{-1} and $S_s = 4.0 \times 10^{-5}$ m^{-1}, respectively. The specific storage was fixed arbitrary to obtain a hydraulic diffusivity value of 10 m^2 s^{-1}. Notice that changing the hydraulic diffusivity value only impacts distances between boundaries and the pumping well. For all models, the early-time display a radial flow regime with relatively negligible well-bore storage. The first model, with two no-flow boundaries (2-NFB) located at 60 m each from the pumping well, displays a slope of 0.5 at intermediate and late-times, which is lower than the observed behavior. The second model, with an additional no-flow boundary (3-NFB) located at 150 m from the pumping well, also displays a slope of 0.5 at at intermediate and late-times. A transition can be observed with a higher slope between 10^3 to 10^4 seconds once the third boundary is reached. The last model, a closed reservoir with an additional no-flow boundary located at 400 m from the pumping well, displays a slope of 1 at intermediate and late-times, which is higher than the observed behavior. These simple modeling scenarios highlight that no-flow boundaries cannot explain the persistent behavior observed at the pumping well.

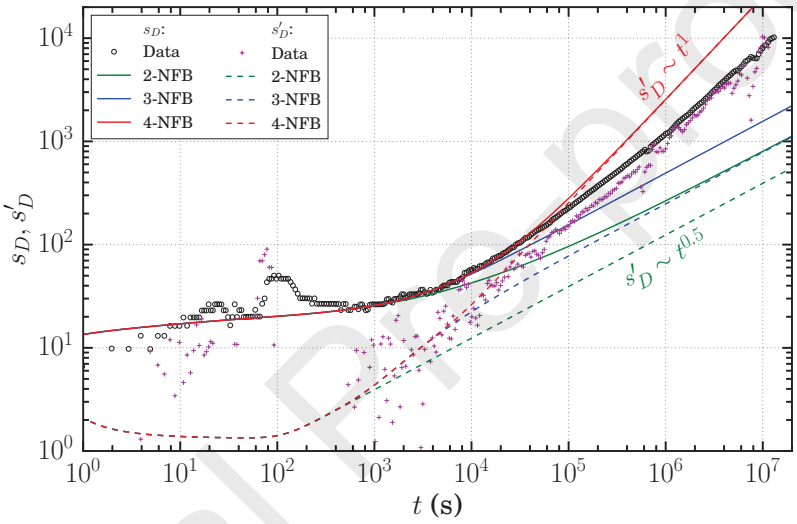

Figure B.9: Normalized drawdowns, s_D, and derivatives, s'_D, for data at the pumping well and models with two no-flow boundaries (2-NFB), three no-flow boundaries (3-NFB), and four no-flow boundaries (4-NFB). The first two boundaries were located at 60 m each from the pumping well. The third and fourth boundaries were located at 150 m and 400 m from the pumping well, respectively.

Appendix C. Numerical model

To evaluate if the equation (6) can be properly used in the present case, where two structures have been highlighted, a simulation has been conducted in an idealized geometry considering two structures with heterogeneous hydraulic properties embedded in an impermeable matrix (Figure C.10). Structure 1 corresponds to the linear feature located at the center of the domain and structure 2 corresponds to the surrounding linear features partly distributed radially from the pumping well. This simulation does not aim to represent the complexity of the site but has the objective to validate if scaling exponents can be properly estimated using the equation (6) for the case of two structures.

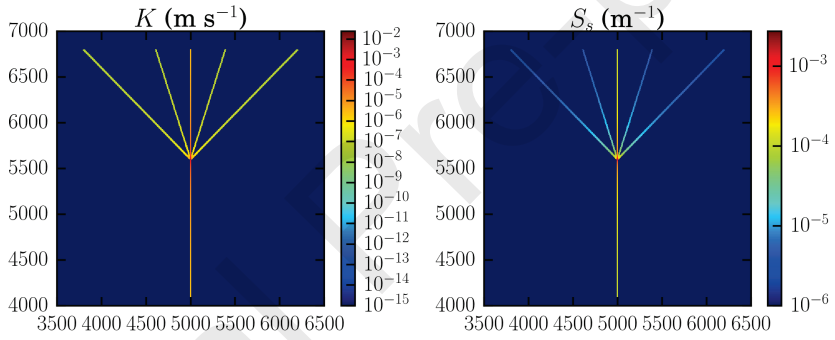

Figure C.10: Distribution of hydraulic conductivity and specific storage in the idealized geometry considering two structures. The pumping well is located at the intersection of the linear features. Structure 1 is represented by the feature at the center of the domain and structure 2 is represented by the surrounding linear features.

Numerical modeling was achieved with Modflow 6, which is based on a generalized control-volume finite-difference approach (Hughes et al., 2017; Langevin et al., 2017, 2018), using the FloPy package (Bakker et al., 2016, 2018). Gridgen program (Lien et al., 2015, 2017) was used to define unstructured quad-tree grids using discretization with vertices in order to improve time calculation. Mesh refinement have been realized at well locations and at the areas of interest, which are the linear features. Multi-aquifer well package was used to define

observation and pumping wells. Well-bore storage and skin effects have been considered at the pumping well in order to fully reproduce the early-time behavior. To simulate skin effects, a cylindrical zone around the pumping well has been defined with a radius of 1 m, a transmissivity of 4.2×10^{-2} m^2 s^{-1}, and a storativity of 2.0×10^{-1}. Simulation was performed assuming a confined system to be consistent with the analytical solution. No-flow boundary conditions were assigned in a sufficiently large domain (i.e., $L_x = 10000$ m and $L_y = 10000$ m) to be of negligible influences during simulation.

To scale hydraulic properties radially from the pumping well, the following equations have been applied:

$$K(r) = K_0 r^{\tau}, \tag{C.1}$$

$$S_s(r) = S_{s0} r^{\sigma}, \tag{C.2}$$

where K_0 [L$^{1-\tau}$ T^{-1}] and S_{s0} [L$^{-1-\sigma}$] are the scaled hydraulic conductivity and specific storage, respectively. The scaling exponents introduced in the model correspond to those extracted from the well test analysis. Table C.3 lists the parameters' values.

Table C.3: Summary of numerical model parameters: τ_i and σ_i are the introduced scaling exponents, K_0 is the scaled hydraulic conductivity, S_{s0} is the scaled specific storage, D_0 is the scaled hydraulic diffusivity, W_d is the width of the linear structures, b is the thickness of the reservoir. The scaling exponents, τ_e and σ_e are extracted from the model output using the scaling analysis procedure.

Str.	τ_i (-)	σ_i (-)	K_0 (m$^{1-\tau}$ s^{-1})	S_{s0} (m$^{-1-\sigma}$)	D_0 (m$^{2+\sigma-\tau}$ s^{-1})	W_d (m)	b (m)	τ_e (-)	σ_e (-)
1	-1.26	-0.44	2.5×10^{-2}	2.8×10^{-3}	9.0×10^{0}	12.5	200	-1.19	-0.45
2	-1.08	-0.96	1.0×10^{-4}	4.3×10^{-3}	2.4×10^{-2}	26.5	200	-1.15	-0.96

The results are presented in Figure C.11, which displays the drawdown behavior for the two structures (Figure C.11, a and b), the characteristic time and amplitude as a function of distance from the pumping well in comparison with

the trends obtained from the well test analysis (Figure C.11, c), and the simulation at the pumping well in comparison with the data (Figure C.11, d). Based on this simple model, the extraction of the scaling exponents with two structures of different hydraulic properties appears to be valid for such contrasted hydraulic properties.

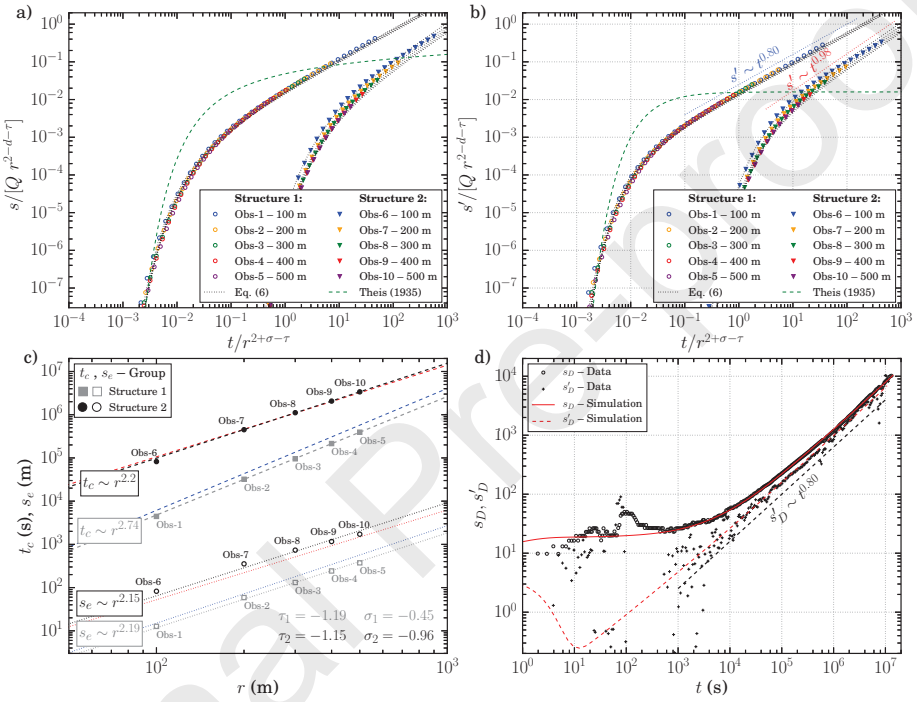

Figure C.11: Results of the numerical model for the idealized structures 1 and 2 geometry: a) Drawdowns, s, and b) derivatives, s', both normalized in time and amplitude according to the respective scaling exponents with fits of the equation (6) using the least-squares method; c) Characteristic time, t_c, and amplitude, s_e, as a function of the distance, r, from the pumping well (colored dashed and dotted lines correspond to the results displayed in Figure 5); d) Normalized drawdowns, s_D, and derivatives, s'_D, for data and model at the pumping well.

References

Acuna, J.A., Yortsos, Y.C., 1995. Application of fractal geometry to the study of networks of fractures and their pressure transient. Water Resources Research 31, 527–540. doi:10.1029/94WR02260.

Ahmadi, M., Gonzalez, O., Ozkan, E., Parsa, E., 2012. Improving well-performance-data analysis in Laplace space by using cubic splines and boundary mirroring. SPE Annual Technical Conference and Exhibition, 8-10 October, San Antonio, Texas, USA SPE–159734. doi:10.2118/159734-MS.

Al-Ajmi, N.M., Ahmadi, M., Ozkan, E., Kazemi, H., 2008. Numerical inversion of Laplace transforms in the solution of transient flow problems with discontinuities. SPE Annual Technical Conference and Exhibition, 21-24 September, Denver, Colorado, USA SPE–116255. doi:10.2118/116255-MS.

Allègre, V., Brodsky, E.E., Xue, L., Nale, S.M., Parker, B.L., Cherry, J.A., 2016. Using earth-tide induced water pressure changes to measure in situ permeability: A comparison with long-term pumping tests. Water Resources Research 52, 3113–3126. doi:10.1002/2015WR017346.

Aydin, A., 1978. Small faults formed as deformation bands in sandstone. Pure and Applied Geophysics 116, 913–930. doi:10.1007/BF00876546.

Aydin, A., 2000. Fractures, faults, and hydrocarbon entrapment, migration and flow. Marine and Petroleum Geology 17, 797–814. doi:10.1016/S0264-8172(00)00020-9.

Bakker, M., Post, V., Langevin, C.D., Hughes, J.D., White, J.T., Starn, J.J., Fienen, M.N., 2016. Scripting MODFLOW model development using Python and FloPy. Groundwater 54, 733–739. doi:10.1111/gwat.12413.

Bakker, M., Post, V., Langevin, C.D., Hughes, J.D., White, J.T., Starn, J.J., Fienen, M.N., 2018. Flopy v3.2.10. U.S. Geological Survey Software Release. doi:10.5066/F7BK19FH.

807 Barker, J.A., 1988. A generalized radial flow model for hydraulic tests in
808 fractured rock. Water Resources Research 24, 1796–1804. doi:10.1029/
809 WR024i010p01796.

810 Bense, V.F., Gleeson, T., Loveless, S.E., Bour, O., Scibek, J., 2013. Fault
811 zone hydrogeology. Earth Science Reviews 127, 171–192. doi:10.1016/j.
812 earscirev.2013.09.008.

813 Bense, V.F., Person, M.A., 2006. Faults as conduit-barrier systems to fluid flow
814 in siliciclastic sedimentary aquifers. Water Resources Research 42, W05421.
815 doi:10.1029/2005WR004480.

816 Berkowitz, B., 2002. Characterizing flow and transport in fractured geological
817 media: A review. Advances in Water Resources 25, 861–884. doi:10.1016/
818 S0309-1708(02)00042-8.

819 Bernard, S., Delay, F., Porel, G., 2006. A new method of data inversion for
820 the identification of fractal characteristics and homogenization scale from hy-
821 draulic pumping tests in fractured aquifers. Journal of Hydrology 328, 647–
822 658. doi:10.1016/j.jhydrol.2006.01.008.

823 Bonnet, E., Bour, O., Odling, N.E., Davy, P., Main, I., Cowie, P., Berkowitz, B.,
824 2001. Scaling of fracture systems in geological media. Reviews of Geophysics
825 39, 347–383. doi:10.1029/1999RG000074.

826 Bourdet, D., Ayoub, J.A., Pirard, Y.M., 1989. Use of pressure derivative in well-
827 test interpretation. SPE Formation Evaluation 4, 293–302, SPE–12777–PA.
828 doi:doi.org/10.2118/12777-PA.

829 Bourgeois, M., Horne, R.N., 1993. Well test model recognition using Laplace
830 space type curves. SPE Formation Evaluation 8, 17–25, SPE–22682–PA.
831 doi:doi.org/10.2118/22682-PA.

832 Bowman II, D.O., Roberts, R.M., Holt, R.M., 2013. Generalized radial flow
833 in synthetic flow systems. Groundwater 51, 768–774. doi:10.1111/j.
834 1745-6584.2012.01014.x.

Carrera, J., Martinez-Landa, L., 2000. Mixed discrete-continuum models: A summary of experiences in test interpretation and model prediction. In Dynamics of Fluid in Fractured Rock, Edited by B. Faybishenko, P.A. Witherspoon, and S.M. Benson AGU, Washington, DC , 251–266.

Carslaw, H.S., Jaeger, J.C., 1959. Conduction of heat in solids. Second Edition, Oxford University Press.

Cello, P.A., Walker, D.D., Valocchi, A.J., Loftis, B., 2009. Flow dimension and anomalous diffusion of aquifer tests in fracture networks. Vadose Zone Journal 8, 258–268. doi:10.2136/vzj2008.0040.

Chang, J., Yortsos, Y.C., 1990. Pressure transient analysis of fractal reservoirs. SPE Reservoir Evaluation & Engineering 5, 31–38, SPE–18170–PA. doi:10.2118/18170-PA.

Cherry, J.A., McWhorter, D.B., Parker, B.L., 2009. Site conceptual model for the migration and fate of contaminants in groundwater at the Santa Susana Field Laboratory, Simi, California. Draft Volumes 1 to 4. Prepared by SSFL Groundwater Advisory Panel in association with the University of Guelph, Montgomery Watson Harza, Haley and Aldrich and AquaResource Inc. URL: https://www.dtsc-ssfl.com/files/lib_rcra_groundwater/SWGWRIR/conceptualmodels/Vol1of4DraftSCMDec09.pdf.

Cherry, J.A., Parker, B.L., Keller, C., 2007. A new depth-discrete multilevel monitoring approach for fractured rock. Ground Water Monitoring & Remediation 27, 57–70. doi:10.1111/j.1745-6592.2007.00137.x.

Cilona, A., Aydin, A., Johnson, N.M., 2015. Permeability of a fault zone cross-cutting a sequence of sandstones and shales and its influence on hydraulic head distribution in the Chatsworth Formation, California, USA. Hydrogeology Journal 23, 405–419. doi:10.1007/s10040-014-1206-1.

Cilona, A., Aydin, A., Likerman, J., Parker, B., Cherry, J., 2016. Structural and statistical characterization of joints and multi-scale faults in an alternating

sandstone and shale turbidite sequence at the Santa Susana Field Laboratory: Implications for their effects on groundwater flow and contaminant transport. Journal of Structural Geology 85, 95–114. doi:10.1016/j.jsg.2016.02.003.

Cinco-Ley, H., Samaniego-V, F., 1981. Transient pressure analysis for fractured wells. Journal of Petroleum Technology 33, 1749–1766, SPE–7490–PA. doi:10.2118/7490-PA.

Copty, N.K., Trinchero, P., Sanchez-Vila, X., 2011. Inferring spatial distribution of the radially integrated transmissivity from pumping tests in heterogeneous confined aquifers. Water Resources Research 47, W05526. doi:10.1029/2010WR009877.

Davy, P., Le Goc, R., Darcel, C., Bour, O., de Dreuzy, J.R., Munier, R., 2010. A likely universal model of fracture scaling and its consequence for crustal hydromechanics. Journal of Geophysical Research: Solid Earth 115, B10411. doi:10.1029/2009JB007043.

Day-Lewis, F.D., Hsieh, P.A., Gorelick, S.M., 2000. Identifying fracture-zone geometry using simulated annealing and hydraulic-connection data. Water Resources Research 36, 1707–1721. doi:10.1029/2000WR900073.

Delay, F., Porel, G., Bernard, S., 2004. Analytical 2D model to invert hydraulic pumping tests in fractured rocks with fractal behavior. Geophysical Research Letters 31, L16501. doi:10.1029/2004GL020500.

Dewandel, B., Aunay, B., Maréchal, J.C., Roques, C., Bour, O., Mougin, B., Aquilina, L., 2014. Analytical solutions for analysing pumping tests in a sub-vertical and anisotropic fault zone draining shallow aquifers. Journal of Hydrology 509, 115–131. doi:10.1016/j.jhydrol.2013.11.014.

Doe, T.W., 1991. Fractional dimension analysis of constant-pressure well tests. SPE Annual Technical Conference and Exhibition, 6-9 October, Dallas, Texas SPE-22702. doi:10.2118/22702-MS.

de Dreuzy, J.R., Davy, P., 2007. Relation between fractional flow models and fractal or long-range 2-D permeability fields. Water Resources Research 43, W04431. doi:10.1029/2006WR005236.

de Dreuzy, J.R., Davy, P., Berkowitz, B., 2001. Advective transport in the percolation backbone in two dimensions. Physical Review E 64, 056305. doi:10.1103/PhysRevE.64.056305.

de Dreuzy, J.R., Méheust, Y., Pichot, G., 2012. Influence of fracture scale heterogeneity on the flow properties of three-dimensional discrete fracture networks (DFN). Journal of Geophysical Research 117, B11207. doi:10.1029/2012JB009461.

Farrell, N., Healy, D., Taylor, C., 2014. Anisotropy of permeability in faulted porous sandstones. Journal of Structural Geology 63, 50–67. doi:10.1016/j.jsg.2014.02.008.

Faulkner, D., Jackson, C., Lunn, R., Schlische, R., Shipton, Z., Wibberley, C., Withjack, M., 2010. A review of recent developments concerning the structure, mechanics and fluid flow properties of fault zones. Journal of Structural Geology 32, 1557–1575. doi:10.1016/j.jsg.2010.06.009.

Ferré, T.P., 2017. Revisiting the relationship between data, models, and decision-making. Groundwater 55, 604–614. doi:10.1111/gwat.12574.

Ferroud, A., Chesnaux, R., Rafini, S., 2018. Insights on pumping well interpretation from flow dimension analysis: The learnings of a multi-context field database. Journal of Hydrology 556, 449–474. doi:10.1016/j.jhydrol.2017.10.008.

Giese, M., Reimann, T., Liedl, R., Maréchal, J.C., Sauter, M., 2017. Application of the flow dimension concept for numerical drawdown data analyses in mixed-flow karst systems. Hydrogeology Journal 25, 799–811. doi:10.1007/s10040-016-1523-7.

Gringarten, A.C., 2008. From straight lines to deconvolution: The evolution of the state of the art in well test analysis. SPE Reservoir Evaluation & Engineering 11, 41–62, SPE–102079–PA. doi:10.2118/102079-PA.

Guéguen, Y., Palciauskas, V., 1994. Introduction to the physics of rocks. Princeton University Press.

Guihéneuf, N., Boisson, A., Bour, O., Dewandel, B., Perrin, J., Dausse, A., Viossanges, M., Chandra, S., Ahmed, S., Maréchal, J.C., 2014. Groundwater flows in weathered crystalline rocks: Impact of piezometric variations and depth-dependent fracture connectivity. Journal of Hydrology 511, 320–334. doi:10.1016/j.jhydrol.2014.01.061.

Guimerà, J., Vives, L., Carrera, J., 1995. A discussion of scale effects on hydraulic conductivity at a granitic site (El Berrocal, Spain). Geophysical Research Letters 22, 1449–1452. doi:10.1029/95GL01493.

Hamm, S.Y., Bidaux, P., 1996. Dual-porosity fractal models for transient flow analysis in fissured rocks. Water Resources Research 32, 2733–2745. doi:10.1029/96WR01464.

Havlin, S., Ben-Avraham, D., 1987. Diffusion in disordered media. Advances in Physics 36, 695–798. doi:10.1080/00018738700101072.

Herrmann, H.J., Stanley, H.E., 1984. Building blocks of percolation clusters: Volatile fractals. Physical Review Letters 53, 1121–1124. doi:10.1103/PhysRevLett.53.1121.

Hughes, J.D., Langevin, C.D., Banta, E.R., 2017. Documentation for the MODFLOW 6 framework. U.S. Geological Survey Techniques and Methods 6, 40. doi:10.3133/tm6A57.

Hurley, J.C., 2003. Rock core investigation of DNAPL penetration and persistence in fractured sandstone. Master's thesis. University of Waterloo, Department of Earth Sciences.

Illman, W.A., 2006. Strong field evidence of directional permeability scale effect in fractured rock. Journal of Hydrology 319, 227–236. doi:10.1016/j.jhydrol.2005.06.032.

den Iseger, P.W., 2006. Numerical transform inversion using Gaussian quadrature. Probability in the Engineering and Informational Sciences 20, 1–44. doi:10.1017/S0269964806060013.

Ishibashi, T., Watanabe, N., Hirano, N., Okamoto, A., Tsuchiya, N., 2015. Beyond-laboratory-scale prediction for channeling flows through subsurface rock fractures with heterogeneous aperture distributions revealed by laboratory evaluation. Journal of Geophysical Research: Solid Earth 120, 106–124. doi:10.1002/2014JB011555.

Jiménez-Martínez, J., Longuevergne, L., Le Borgne, T., Davy, P., Russian, A., Bour, O., 2013. Temporal and spatial scaling of hydraulic response to recharge in fractured aquifers: Insights from a frequency domain analysis. Water Resources Research 49, 3007–3023. doi:10.1002/wrcr.20260.

Jourde, H., Cornaton, F., Pistre, S., Bidaux, P., 2002a. Flow behavior in a dual fracture network. Journal of Hydrology 266, 99–119. doi:10.1016/S0022-1694(02)00120-8.

Jourde, H., Pistre, S., Perrochet, P., Drogue, C., 2002b. Origin of fractional flow dimension to a partially penetrating well in stratified fractured reservoirs. New results based on the study of synthetic fracture networks. Advances in Water Resources 25, 371–387. doi:10.1016/S0309-1708(02)00010-6.

Kaczmaryk, A., Delay, F., 2007. Interference pumping tests in a fractured limestone (Poitiers – France): Inversion of data by means of dual-medium approaches. Journal of Hydrology 337, 133–146. doi:10.1016/j.jhydrol.2007.01.025.

Karasaki, K., Long, J.C.S., Witherspoon, P.A., 1988. Analytical mod-

els of slug tests. Water Resources Research 24, 115–126. doi:10.1029/WR024i001p00115.

Kikuchi, C.P., Ferré, T.P.A., Vrugt, J.A., 2015. On the optimal design of experiments for conceptual and predictive discrimination of hydrologic system models. Water Resources Research 51, 4454–4481. doi:10.1002/2014WR016795.

Langevin, C.D., Hughes, J.D., Banta, E.R., Niswonger, R.G., Panday, S., Provost, A.M., 2017. Documentation for the MODFLOW 6 groundwater flow model. U.S. Geological Survey Techniques and Methods 6, 197. doi:10.3133/tm6A55.

Langevin, C.D., Hughes, J.D., Banta, E.R., Provost, A.M., Niswonger, R.G., Panday, S., 2018. Modflow 6 modular hydrologic model version 6.0.3. U.S. Geological Survey Software Release. doi:10.5066/F76Q1VQV.

Le Borgne, T., Bour, O., de Dreuzy, J.R., Davy, P., Touchard, F., 2004. Equivalent mean flow models for fractured aquifers: Insights from a pumping tests scaling interpretation. Water Resources Research 40, W03512. doi:10.1029/2003WR002436.

Lei, Q., Latham, J.P., Tsang, C.F., 2017. The use of discrete fracture networks for modelling coupled geomechanical and hydrological behaviour of fractured rocks. Computers and Geotechnics 85, 151–176. doi:10.1016/j.compgeo.2016.12.024.

Levitan, M., 2005. Practical application of pressure/rate deconvolution to analysis of real well tests. SPE Reservoir Evaluation & Engineering 8, 113–121, SPE–84290–PA. doi:10.2118/84290-PA.

Lien, J.M., Liu, G., Langevin, C.D., 2015. GRIDGEN version 1.0 – A computer program for generating unstructured finite-volume grids. U.S. Geological Survey Open-File Report 2014-1109, 26. doi:10.3133/ofr20141109.

Lien, J.M., Liu, G., Langevin, C.D., 2017. GRIDGEN version 1.0.02 – a computer program for generating unstructured finite-volume grids. U.S. Geological Survey Software Release. doi:10.5066/F79G5JXV.

Link, M.H., Squires, R.L., Colburn, I.P., 1984. Slope and deep-sea fan facies and paleogeography of Upper Cretaceous Chatsworth Formation, Simi Hills, California. AAPG Bulletin 68, 850–873.

Liu, M.M., Chen, Y.F., Hong, J.M., Zhou, C.B., 2016. A generalized non-Darcian radial flow model for constant rate test. Water Resources Research 52, 9325–9343. doi:10.1002/2016WR018963.

Lods, G., Gouze, P., 2004. WTFM, software for well test analysis in fractured media combining fractional flow with double porosity and leakance approaches. Computers & Geosciences 30, 937–947. doi:10.1016/j.cageo.2004.06.003.

Lods, G., Gouze, P., 2008. A generalized solution for transient radial flow in hierarchical multifractal fractured aquifers. Water Resources Research 44, W12405. doi:10.1029/2008WR007125.

Maillot, J., Davy, P., Le Goc, R., Darcel, C., de Dreuzy, J.R., 2016. Connectivity, permeability, and channeling in randomly distributed and kinematically defined discrete fracture network models. Water Resources Research 52, 8526–8545. doi:10.1002/2016WR018973.

Manna, F., Cherry, J.A., McWhorter, D.B., Parker, B.L., 2016. Groundwater recharge assessment in an upland sandstone aquifer of southern California. Journal of Hydrology 541, 787–799. doi:10.1016/j.jhydrol.2016.07.039.

de Marsily, G., 1986. Quantitative hydrogeology: Groundwater hydrology for engineers. San Diego, California: Academic Press.

Méheust, Y., Schmittbuhl, J., 2001. Geometrical heterogeneities and permeability anisotropy of rough fractures. Journal of Geophysical Research: Solid Earth 106, 2089–2102. doi:10.1029/2000JB900306.

Moench, A.F., 1984. Double-porosity models for a fissured groundwater reservoir with fracture skin. Water Resources Research 20, 831–846. doi:10.1029/WR020i007p00831.

MWH, 2004. Results of C-1 pumping test. In Appendix K, Phase I of northeast investigation area groundwater characterization, Santa Susana Field Laboratory, Ventura County, California. Technical Report. Prepared for The Boeing Company, National Aeronautics and Space Administration, and U.S. Department of Energy. URL: https://www.dtsc-ssfl.com/files/lib_rcra_soils/group5/historicaldocs/PDF_Files/HDMSe00123605.pdf.

MWH, 2007. Geologic characterization of the central Santa Susana Field Laboratory, Ventura County, California. Technical Report. Prepared for The Boeing Company, National Aeronautics and Space Administration, and U.S. Department of Energy. URL: https://www.dtsc-ssfl.com/files/lib_rcra_groundwater/rfi_reports/rfireports/225_GeologyReport2007FINAL.pdf.

MWH, 2016. Hydrogeologic characterization of faults, Santa Susana Field Laboratory, Ventura County, California. Technical Report. Prepared for The Boeing Company, National Aeronautics and Space Administration, and U.S. Department of Energy. URL: https://www.dtsc-ssfl.com/files/lib_rcra_groundwater/faults/2016_11_Draft_Hydrogeologic_Characterization_of_SSFL_Faults_Nov_2016_portfolio.pdf.

National Research Council, 1996. Rock fractures and fluid flow: Contemporary understanding and applications. The National Academies Press, Washington, D.C.

Odling, N.E., West, L.J., Hartmann, S., Kilpatrick, A., 2013. Fractional flow in fractured chalk; a flow and tracer test revisited. Journal of Contaminant Hydrology 147, 96–111. doi:10.1016/j.jconhyd.2013.02.003.

Olsson, O., Gale, J.E., 1995. Site assessment and characterization for high-level nuclear waste disposal: results from the Stripa Project, Sweden. Quarterly

Journal of Engineering Geology and Hydrogeology 28, S17–S30. doi:10.1144/GSL.QJEGH.1995.028.S1.02.

Oron, A.P., Berkowitz, B., 1998. Flow in rock fractures: The local cubic law assumption reexamined. Water Resources Research 34, 2811–2825. doi:10.1029/98WR02285.

O'Shaughnessy, B., Procaccia, I., 1985. Diffusion on fractals. Physical Review A 32, 3073–3083. doi:10.1103/PhysRevA.32.3073.

Papadopulos, I.S., Cooper, H.H., 1967. Drawdown in a well of large diameter. Water Resources Research 3, 241–244. doi:10.1029/WR003i001p00241.

Pedretti, D., Russian, A., Sanchez-Vila, X., Dentz, M., 2016. Scale dependence of the hydraulic properties of a fractured aquifer estimated using transfer functions. Water Resources Research 52, 5008–5024. doi:10.1002/2016WR018660.

Pham, H.V., Tsai, F.T.C., 2016. Optimal observation network design for conceptual model discrimination and uncertainty reduction. Water Resources Research 52, 1245–1264. doi:10.1002/2015WR017474.

Pimonov, E.A., Onur, M., Kuchuk, F.J., 2009. A new robust algorithm for solution of pressure/rate deconvolution problem. Journal of Inverse and Ill-posed Problems 17, 611–627. doi:10.1515/JIIP.2009.038.

Quinn, P., Cherry, J.A., Parker, B.L., 2015. Combined use of straddle packer testing and FLUTe profiling for hydraulic testing in fractured rock boreholes. Journal of Hydrology 524, 439–454. doi:10.1016/j.jhydrol.2015.03.008.

Quinn, P., Cherry, J.A., Parker, B.L., 2016. Straddle packer testing at the Santa Susana Field Laboratory, Ventura County, California. Technical Report. Prepared for The Boeing Company.

Rafini, S., Larocque, M., 2009. Insights from numerical modeling on the hydrodynamics of non-radial flow in faulted media. Advances in Water Resources 32, 1170–1179. doi:10.1016/j.advwatres.2009.03.009.

Rasmussen, T.C., Crawford, L.A., 1997. Identifying and removing barometric pressure effects in confined and unconfined aquifers. Groundwater 35, 502–511. doi:10.1111/j.1745-6584.1997.tb00111.x.

Renard, P., Glenz, D., Mejias, M., 2009. Understanding diagnostic plots for well-test interpretation. Hydrogeology Journal 17, 589–600. doi:10.1007/s10040-008-0392-0.

Romboutsos, A., Stewart, G., 1988. A direct deconvolution or convolution algorithm for well test analysis. SPE Annual Technical Conference and Exhibition, 2-5 October, Houston, Texas, USA SPE 18157. doi:10.2118/18157-MS.

Roques, C., Bour, O., Aquilina, L., Dewandel, B., Leray, S., Schroetter, J., Longuevergne, L., Le Borgne, T., Hochreutener, R., Labasque, T., Lavenant, N., Vergnaud-Ayraud, V., Mougin, B., 2014. Hydrological behavior of a deep sub-vertical fault in crystalline basement and relationships with surrounding reservoirs. Journal of Hydrology 509, 42–54. doi:10.1016/j.jhydrol.2013.11.023.

Savage, H.M., Brodsky, E.E., 2011. Collateral damage: Evolution with displacement of fracture distribution and secondary fault strands in fault damage zones. Journal of Geophysical Research: Solid Earth 116, B03405. doi:10.1029/2010JB007665.

von Schroeter, T., Hollaender, F., Gringarten, A.C., 2004. Deconvolution of well-test data as a nonlinear total least-squares problem. SPE Journal 9, 375–390, SPE–77688–PA. doi:10.2118/77688-PA.

Stewart, G., 2011. Well test design & analysis. PennWell Corporation.

Theis, C.V., 1935. The relation between the lowering of the piezometric surface and the rate and duration of discharge of a well using ground-water storage. Eos, Transactions American Geophysical Union 16, 519–524. doi:10.1029/TR016i002p00519.

Vesselinov, V.V., Neuman, S.P., Illman, W.A., 2001. Three-dimensional numerical inversion of pneumatic cross-hole tests in unsaturated fractured tuff: 1. Methodology and borehole effects. Water Resources Research 37, 3001–3017. doi:10.1029/2000WR000133.

Walker, D.D., Cello, P.A., Valocchi, A.J., Loftis, B., 2006. Flow dimensions corresponding to stochastic models of heterogeneous transmissivity. Geophysical Research Letters 33, L07407. doi:10.1029/2006GL025695.

Warren, J.E., Root, P.J., 1963. The behaviour of naturally fractured reservoirs. Society of Petroleum Engineers Journal 3, 245–255, SPE–426–PA. doi:10.2118/426-PA.

Zech, A., Müller, S., Mai, J., Heße, F., Attinger, S., 2016. Extending Theis' solution: Using transient pumping tests to estimate parameters of aquifer heterogeneity. Water Resources Research 52, 6156–6170. doi:10.1002/2015WR018509.

Zhang, Q., Wang, X., Wang, D., Zeng, J., Zeng, F., Zhang, L., 2018. Pressure transient analysis for vertical fractured wells with fishbone fracture patterns. Journal of Natural Gas Science and Engineering 52, 187–201. doi:10.1016/j.jngse.2018.01.032.